Correlation between the relative blob fraction and plasma parameters in NSTX

S. J. Zweben, S. Banerjee, N. Bisai, et al.

View Online   Export Citation   CrossMark

Correlation between the relative blob fraction and plasma parameters in NSTX

View Online   Export Citation   CrossMark

S. J. Zweben,[1,a] (iD) S. Banerjee,[1] (iD) N. Bisai,[2,3] (iD) A. Diallo,[1] (iD) M. Lampert,[1] (iD) B. LeBlanc,[1] J. R. Myra,[4] (iD)
and D. A. Russell[4] (iD)

AFFILIATIONS

[1]Princeton Plasma Physics Laboratory, Princeton, New Jersey 08540, USA
[2]Institute for Plasma Research, Bhat, Gandhinagar 382428, India
[3]Homi Bhabha National Institute (HBNI), Anushakti Nagar, Mumbai, Maharashtra 400094, India
[4]Lodestar Research Corporation, Boulder, Colorado 80301, USA

[a]Author to whom correspondence should be addressed: stewart.zweben@gmail.com

ABSTRACT

This paper presents a simple analysis of the fraction of blobs observed in the scrape-off layer of NSTX and calculates the correlation between this blob fraction and various plasma parameters. The measurements were made using the gas puff imaging (GPI) diagnostic on a database of 103 shots from 2010 with neutral beam power $P_{NBI} = 0-6$ MW. The blob fraction ranged from $f_b = 0.1\%$ to 4.8%, where f_b is defined as the fraction of time the GPI signal was larger than three times its average value within 0–7.5 cm outside the separatrix. The blob fraction generally decreased with increasing neutral beam injection power and was lower on average in H-mode plasmas than Ohmic and L-mode plasmas. The blob fraction had its highest correlation with the measured poloidal turbulence velocity and its radial gradient just inside the separatrix. This is in part consistent with a model in which the blob generation rate increases with the poloidal velocity shear.

I. INTRODUCTION

Blobs are turbulent filamentary structures in the scrape-off layer (SOL) of tokamaks and other magnetized plasmas. Blobs are important since they carry heat and particles radially across the SOL, and so, at least in part, determine the SOL width and local erosion of the walls or divertor plates. Although the basic mechanism of radial blob motion was discovered in 2001[1] and a theoretical criterion for blob formation was presented in 2005,[2] by 2010 there was still only a partial connection between theory and experiment.[3] A list of experimental and theoretical references prior to 2011 can be found in Ref. 3.

Since 2011, there has been good progress in the experimental study of blobs in tokamaks. For example, the 3D structure of these B-field aligned blob filaments has been clarified using wide-angle high-speed imaging in MAST[4] and analyses of these images show that the blob filaments are randomly emitted from the core in a toroidally uniform way along the separatrix in the midplane region without a clear modal structure.[5] The role of blobs in linking the divertor collisionality with perpendicular SOL transport was established in ASDEX and JET,[6] and probe measurements in ASDEX Upgrade and TCV (Tokamak a Configuration Variable) in the L-mode have shown a

relationship between the blob size and the SOL density e-folding length.[7] The radial and poloidal motion of blobs in the SOL of HL-2A was well correlated with the floating potential gradients determining the E × B velocity.[8] Extensive analysis of blobs in NSTX was done using gas puff imaging (GPI) data,[9,10] as described further below, and blob dynamics has also been studied in detail in non-tokamak devices such as TORPEX.[11]

There has also been significant progress in the theory and simulation of blobs in tokamaks, even in just the past two years. For example, agreement between analytic and numerical results on blob velocity scaling in diverted tokamaks was found using the GBS fluid code.[12] Simulations using the BOUT++ code showed that blobs are generated near the peak pedestal pressure gradient region inside the separatrix and contribute to the transport of the particle and heat in the SOL region.[13] Blobs have been identified in gyrokinetic simulations of DIII-D and C-Mod using the XGC-1 code.[14] Blob–blob interactions were studied in 2D SOL simulations[15] and in 3D simulations including divertor geometry.[16] A universal analytic criterion for blob birth was proposed[17] and recently extended to finite electron temperature effects.[18]

Despite this recent progress in blob physics, it is still not clear what determines the frequency or number of blobs in the SOL for a

particular type of tokamak discharge condition. Which plasma parameters correlate best with the population of blobs?

Some experimental results on this topic can be found in the existing literature. For example, an early paper using Langmuir probes in DIII-D showed larger amplitude blobs in L-mode than in H-mode plasmas,[19] and an early study of the "packing fraction" and linear density of blobs using GPI in NSTX showed more blobs just outside the separatrix in the L-mode than in the H-mode.[20] However, the statistical properties of edge turbulence were the same in both L-mode and H-mode as measured by probes at the bottom of USN (upper single null) discharges in ASDEX-Upgrade.[21] An increase in the generation rate of blobs was seen during edge biasing in the CASTOR tokamak and was attributed to increased poloidal velocity shear,[22] while the blob generation rate was measured in ASDEX-Upgrade and explained by a model based on the edge density and temperature profiles.[23] Blob size and lifetime were observed to increase with line-averaged density in L-mode discharges in ASDEX-Upgrade,[6] but the statistical properties of blobs as measured by GPI in the SOL of Alcator C-Mod were the same in high and low density Ohmic discharges and in H-mode plasmas.[24] The blob size in MAST as measured with passive imaging showed a slight increase with plasma current,[25] while the blob size and radial velocity as measured with probes in Ohmic L-mode plasmas in TCV showed a wide variation as a function of edge collisional frequency.[26] In summary, it is not yet clear from previous experimental results which plasma parameters correlate best with the relative population of blobs in tokamaks.

The goal of the present paper is to characterize and understand the relative blob fraction in a wide database of NSTX discharges using GPI measurements in the SOL. This paper is an extension of a previous paper on blob statistics in NSTX,[9] which used GPI data from many of the same discharges. Although that paper contained a multivariable analysis of blobs over a wide database, the results were complicated and difficult to interpret. The present paper uses a simplified blob definition and a more carefully chosen database to provide a single blob fraction estimate for each shot. The present paper also includes a wider radial range of analysis of the Thomson scattering and GPI turbulence velocity, and the results are interpreted using newly applied theory and simulations.

The GPI diagnostic, database, and blob analysis methods are described in Sec. II. Section III describes the new results, including the correlation of relative blob fractions with global and local plasma parameters. Section IV discusses these results and tries to put them into a theoretical framework, and Sec. V summarizes the conclusions.

II. GPI DIAGNOSTIC, DATABASE, AND DATA ANALYSIS

This section gives an overview of the GPI diagnostic in Sec. II A and then describes the GPI database selection process for the present paper in Sec. II B. The two blob analysis methods used here are described in Sec. II C, with the results described in Secs. III A and III B. Three videos of the raw GPI camera data are shown in the supplementary material, and more examples can be found online in Ref. 27.

A. GPI diagnostic

The GPI diagnostic of NSTX has been described in previous papers;[9,10] so, only a brief summary is presented here. In GPI, a fast camera (Vision Research Phantom 710) views a deuterium neutral gas cloud puffed into the edge plasma, using a Dα filter to image a neutral

deuterium emission line during the steady-state part of the discharge. This neutral gas cloud increases the Dα emission within the camera line of sight by a factor of at least 10 over a distance of about 12 cm along the B field line, which localizes this line emission to the region near the gas puffer. The camera viewing angle is as near as possible aligned along the local magnetic field, which is tilted at an angle of about 36° with respect to the toroidal direction in NSTX, resulting in images of the local Dα light emission from the cloud that are approximately radial (i.e., perpendicular to the local separatrix) vs poloidal or "binormal" (i.e., along the local separatrix). The camera images all have 64 × 80 pixels at 400 000 frames/s (2.5 μs/frame).

This GPI camera views an area about 24 cm radially and 30 cm poloidally, i.e., normal and binormal to the local magnetic field and centered just above the outer midplane. Most of the GPI light emission occurs within ±5 cm of the separatrix where the electron temperature is high enough to excite the Dα line but low enough so that the neutrals are not completely ionized (roughly $T_e \sim 10$–200 eV). The single GPI gas puff per shot produces usable Dα signal over ~50 ms, but for this paper only a 10 ms period centered at the time of the peak of the total GPI signal is analyzed.

The Dα light emission seen in GPI can fluctuate due to the local electron density and temperature variations, including both turbulent and coherent fluctuations. For the present blob fraction measurements in the SOL of NSTX where (almost always) $n_e < 1 \times 10^{13}$ cm^{-3} and $T_e < 100$ eV, the GPI signal is nearly linear with the local electron density and nearly independent of the electron temperature.[28] Thus, these GPI fluctuations in the SOL of NSTX can be assumed to be proportional to the local electron density, at least to a first approximation.

The present analysis is done using the Dα light emission itself with no attempt to unfold the underlying electron density, temperature, or possible neutral density fluctuations. Various issues and assumptions in the analysis and interpretation of these GPI images were discussed in a GPI diagnostic review paper.[28] For example, slight misalignments of the camera view with respect to the local B field line are not taken into account here, and neutral density fluctuations are unlikely due to the low density and temperature in the SOL. The GPI data cannot be used to determine the turbulent transport, so there is no discussion of the heat or particle SOL widths. However, the GPI diagnostic is well suited for the identification and analysis of blobs in the SOL, which is the topic of the present paper.

B. Database

The database of 103 NSTX discharges used for the present paper was selected from the full 300-shot database of 2010 GPI data using the following criteria. First, a consistent time period of interest of ±5 ms around the peak time of the GPI signal was chosen to provide the largest possible signal levels (see Sec. II A). Then, any H-mode shot with one or more clear ELM event during this time period was eliminated (97 shots). Shots with low frequency MHD-induced modulation in the GPI signal were then eliminated (38 shots), including the seven H-mode shots previously used in an Ohmic vs H-mode comparison[9] that were recently identified as having a blob–MHD correlation.[29] Shots with RF heating were excluded (23 shots), since RF heating has a complex and largely unknown effect on the edge plasma. Also removed were shots with transient events such as L–H transitions or changes in applied power or plasma edge radius (24 shots), shots with a small (≤7.5 cm) outer gap between the local separatrix and the RF

antenna limiter (six shots), and shots with inadequate EFIT results (nine shots).

This database covers the full range of NSTX parameters, as shown in Table I, with toroidal field B = 3.4–5.4 kG, plasma current I = 0.6–1.2 MA, line-averaged density n = 1.4–7.2 × 10^{13} cm^{-3}, plasma stored energy W = 18–325 kJ, neutral beam injection (NBI) injected power P = 0–6.1 MW, and plasma energy confinement time τ_E = 14–103 ms. All shots were fueled with deuterium. Thirty shots had only Ohmic heating, 15 were in the L-mode with low NBI power, and 58 were in the H-mode with high NBI power. The plasma shape was normally lower single null divertor with a vertical elongation of κ = 1.9–2.6 and an outer midplane separatrix radius of R_{sep} = 142.6–150.8 cm. Within the GPI field of view, there was a variable outer gap of ∼7–15 cm between the local separatrix and the RF antenna shadow, the innermost edge of which was located at R = 157.5 cm at the outer midplane. Over this 8 cm range in the separatrix radius, the present GPI imaging is equally effective and the results are directly comparable.

This database of 103 shots was more restrictive than the earlier database of 140 shots in the analysis of Ref. 9. The present database includes 76 shots that were in the previous database along with 27 new shots. Of these 27 new shots, 21 were not used previously used since they were similar to other shots in the previous database, five were not used previously because they had a slightly low ratio of I/B (acceptable for the present database), and one shot had its separatrix slightly too near the inner edge of the GPI view (not important for the present database). Of the 140 shots in the previous database, 32 were not used in the present database due to the presence of small ELMs, 17 were not used due to MHD activity, five were not used due to RF heating, four were not used due to a small outer gap, and six were not used due to transient events or drifts during the time of interest.

In summary, the primary variable in the present database is the NBI heating power, with minimal variations due to ELMs, MHD, or RF power. All available shots from the 2010 run that met the criterion of the first paragraph were used in this database.

C. Blob analyses: Threshold and contour definitions

Various algorithms have previously been used to define blobs in the context of theory, computational simulations, and experiments, depending on the type of data analyzed and the physics goals.[3] For

TABLE I. Database parameters and sample shots.

Parameter	103 shots	#142 270	#138 121	#141 324
Shot type	OH, L, H	L-mode	Ohmic	H-mode
GPI time (ms)	162–814	372	226	532
Bt (kG)	3.4–5.4	4.4	4.4	4.4
Ip (MA)	0.6–1.2	0.79	0.9	0.65
P_{NBI} (MW)	0–6.1	1.0	0	2.9
Outer gap (cm)	6.7–14.9	8.2	9.8	13.1
W (kJ)	18–325	68	35	143
n (10^{13} cm^{-3})	1.4–7.2	3.3	1.9	5.1
τ_E (ms)	14–103	32	32	51
Blob fraction	0.12%–4.84%	3.2%	4.7%	0.6%

example, blobs in 2D simulations were defined using image processing and blob tracking,[15] while single-point probe measurements often use a threshold of 2.5 times the standard deviation.[19] Every definition is somewhat arbitrary since there is no sharp dividing line between the blobs and background turbulence, and since blobs evolve over time with variable size and shape and with different relative perturbations in density, potential, and temperature. Therefore, the blob analysis results in this paper (and elsewhere) provide only a *relative* measure of the blobs calculated using a specific definition.

The present blob analysis starts by normalizing (i.e., dividing) each GPI frame by the time-average of all GPI frames over the 10 ms time of interest for that shot. This allows the identification of blobs as space/time regions with a much higher-than-average GPI signal, and removes spatial variations due the Dα emission profile, the pixel-to-pixel camera sensitivity, and optical vignetting. Slow variations (<1 kHz) due to the gas puff time evolution are then filtered out from the camera signals, so that for each separate pixel the normalized signal averages very near 1.0 over every 1 ms time interval. The next step is to smooth the image over ±1 pixels in space in both directions to reduce noise, which is appropriate since the pixel size is 0.375 cm × 0.375 cm radial × poloidal and the optical resolution is ∼1 cm. No corrections are made for spatial distortion due to slight misalignments of GPI view with the local B field,[30] since this mainly changes the blob shape and not its normalized amplitude. To reduce the effects of random noise in pixels with very small GPI signals, pixels with a camera output level below 10 camera signal units are not used in the analysis, where for reference the maximum signals in the time-averaged images range from 125 to 640 camera signal units for shots in this database.

The "blob fraction" is defined in two different ways in this paper. The first and primary definition is the fraction of time that the *normalized* GPI signal is above a threshold level of T = 3, averaged over the spatial region of interest in the SOL. This blob fraction is, thus, a simple way to measure the degree of large amplitude fluctuations in the probability distribution function (PDF) of the normalized GPI signals. Note that this definition does not keep track of the location or shape of the blobs within this region, but just counts for each pixel the number of frames that have at a signal level at least T = 3 times the time-averaged signal level for that pixel, and then averages this fraction over all pixels in the spatial region of interest.

Mathematically, this primary definition of the blob fraction can be written as

$$f_b = \text{blob fraction} = \sum\nolimits_{x,y,t} N_{pix}(\text{above } T = 3) / \sum\nolimits_{x,y,t} N_{pix}(\text{all}),$$

(1)

where the sum is taken over the spatial region of interest (blob analysis zone) from x = 0–7.5 cm (or 0–20 columns) radially outside the separatrix, y = ±11.5 cm (the 60 rows #10–69) poloidally from the vertical center of the GPI images, and over the time range t = 10 ms (or ∼4000 frames) of interest. Here, N_{pix} (above T = 3) is the number of frames with a signal amplitude above the normalized threshold level of T = 3 for each pixel, then summed over all pixels in this region, and N_{pix} (all) is the total number of all pixels in all frames in this space–time region (i.e., N_{pix} ∼ 21 radial × 60 poloidal × 4000 time = 5 × 10^6). Signal normalization ensures that the time-averaged amplitude in each pixel is very near 1.0. Note that this blob fraction analysis does not identify or track the shape or amplitude of individual blobs.

Note that this blob analysis region moves radially with the local separatrix in the GPI field of view and retains a radial width of 7.5 cm for all shots. The analysis region extends radially out to the edge of the RF antenna limiter shadow for some shots, but not radially beyond the RF limiter shadow.

The blob fraction as defined in Eq. (1) can also be interpreted as the probability of finding a large amplitude fluctuation (blob) at some point in the region of interest. It is proportional to the blob generation rate and to the duration of time the blob spends in the SOL, but it is much more easily and accurately calculated than either of these two quantities separately. The threshold of $T = 3$ corresponds to 2.5× the standard deviation when the standard deviation divided by the mean is 0.80. Note that the chosen threshold of $T = 3$ counts only relatively large blob fluctuations; for example, if the GPI signal always stays below three times its time-averaged value, then the blob fraction is $f_b = 0$. Examples of the calculation of blob fraction for specific shots in NSTX are discussed in Sec. III A.

The blob fraction as defined here is simply a convenient and robust measurement of the relative blob population among different types of discharges as measured using GPI in NSTX. The same blob fraction calculation could be done on other machines and/or with other diagnostics; however, the absolute values of f_b for a given plasma will depend on the diagnostic sensitivities. The main utility of these blob fraction measurements at present is to assist in the validation of theoretical models for blob formation in tokamaks, as discussed in Sec. IV.

Blobs were also identified in a second (and secondary) way as individual 2D regions within which the GPI signal level exceeded the normalized signal threshold of $T = 3$. The minimum contiguous area required for a blob to be identified was 10 pixels in area or $1.4 \, cm^2$. These contiguous regions were found using the "contour" function in IDL operating on a re-binned GPI image of 10× its original pixel numbers, i.e., 640×800. Only closed contours, which did not overlap the edge of the frame, with centers in the region defined above were counted as blobs. More than one non-overlapping blob can be identified in each frame; however, most frames have only 0 or 1 blob (see Sec. III B). The blob center was calculated from the horizontal and vertical mean of the circumferential contours, and the blob area was calculated using the "shoelace formula."[31]

The second blob fraction method using contours was used only as a check of the first blob fraction method done using the $T = 3$ threshold. These two methods agreed well with each other, as described in Sec. III B, but the first method was used for the majority of the data analysis since it was simpler and easier to apply to the theoretical models for the comparisons with experimental data, as discussed in Sec. IV.

III. BLOB ANALYSIS RESULTS

This section presents the results for the relative blob fractions in this NSTX GPI database, including trends with respect to global and local plasma parameters. Section III A describes results from the simplest measure of blob fraction based on a threshold in the normalized GPI signal levels, including trends in the blob fraction with respect to global plasma parameters. Section III B describes the alternative analysis using contour mapping and compares the results with the threshold analysis. Section III C analyzes trends in the blob fraction with respect to edge parameters from Thomson scattering, and Sec. III D analyzes trends in the blob fraction with respect to the edge poloidal turbulence velocity derived from GPI data. Further discussion of these results is presented in Sec. IV.

A. Blob fraction from PDF threshold

Figure 1(a) shows the time-average of the raw GPI camera images over ±5 ms around the peak of the GPI signal (372 ms) for a typical L-mode shot (#142 270), where the separatrix is shown by a dashed white line, and the GPI gas manifold is shown as a solid white line. The plasma parameters for this shot are listed in Table I. The GPI images in Fig. 1(a) cover over 24 cm in the radial (horizontal) direction and 30 cm in the poloidal or binormal direction (vertical), and this same region is viewed for all shots.

The GPI Dα signal in Fig. 1(a) peaks about 1 cm inside the separatrix for this shot, where the red temperature color scale ranges from 0 to 460 in units of camera output. Figure 1(b) shows a single 2.5 μs frame taken during this time in which a blob is found a few centimeters outside the separatrix. Figure 1(c) shows the same frame as in Fig. 1(b) but in a normalized image with a blue color scale from 0 (black) to 10 (white), which highlights the blob. A movie of the raw
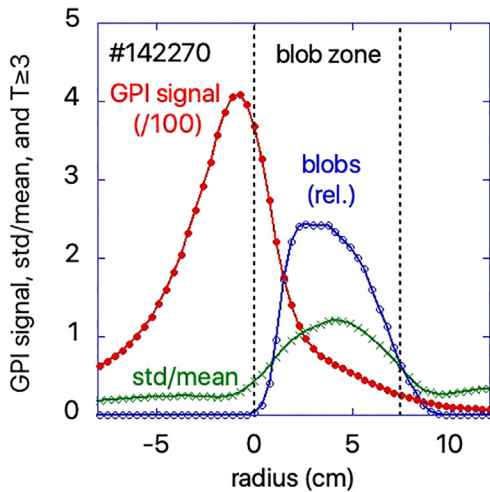

| (a) average image | (b) blob image | (c) norm. blob | (d) blob % (rel) |
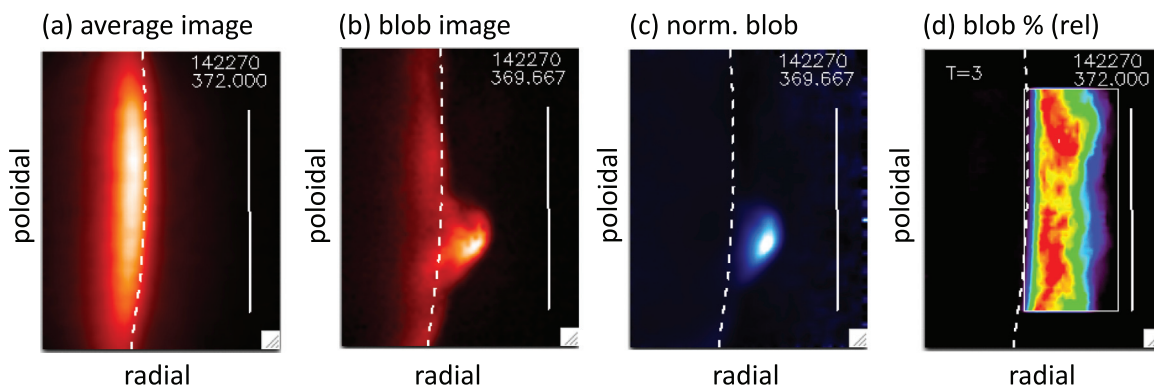
FIG. 1. (a) Image showing the time-averaged GPI signal level for shot #142 270 along with the local separatrix (dashed white line), and the GPI gas manifold (solid white line). The signal level peaks about 1 cm inside the separatrix. (b) Single frame with a blob in the same color scale and figure (c) this same frame in a normalized image with a blue color scale of 0 (black) to 10 (white). (d) Relative number of frames having a normalized signal level ≥ 3 (red = 6%), along with a white box showing the blob analysis region used for this paper.

camera data vs time for 2 ms in this shot can be found in the supplementary material.

Figure 1(d) shows a map of the same GPI region with a color code showing the relative fraction of pixels during the 10 ms of interest having a normalized signal level of ≥ 3, where the threshold level $T = 3$ is used to define a blob (see Sec. II B). The color scale here ranges from 0% (black) to 6% (red), as evaluated for each pixel separately. The blob analysis region within the white box extends 7.5 cm (20 pixels) radially and ± 11.25 cm (rows #10–69) poloidally from the vertical center of the GPI image at the separatrix. Blobs defined this way are fairly uniformly distributed in the poloidal direction, with the blob fraction peaking a few cm radially outside the separatrix (red colored areas).
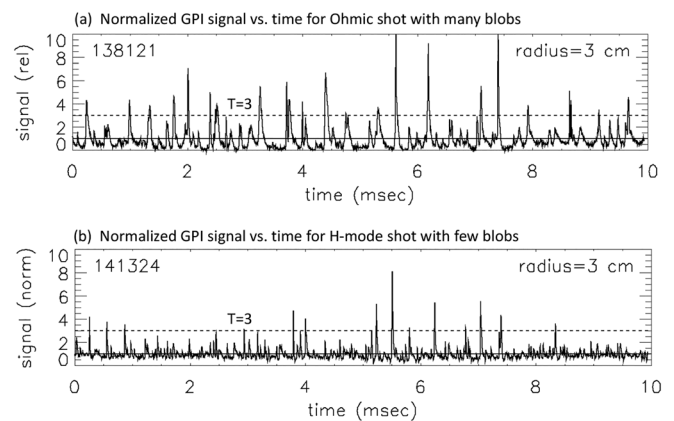
Figure 2 shows more clearly the radial profile of the time-averaged GPI signal of Fig. 1(a), averaged over rows #10–69 in the image data and divided by 100 (red curve). This horizontal axis is the distance from the separatrix at the vertical middle of the image. The raw GPI signal peaks about 1 cm inside the separatrix in this shot, and the region of blob analysis from 0 to 7.5 cm outside the separatrix is labeled the "blob zone." The blue curve in Fig. 2 shows the radial profile of the relative number of pixels with a normalized signal level of ≥ 3 within the vertical range of rows #10–69 (on a relative scale). The maximum of this blue curve occurs at 2–4 cm outside the separatrix for this shot, and the total blob fraction for this shot (averaged over the blob zone) is $f_b = 3.2\%$. For reference, the green curve shows the relative GPI signal fluctuation level (standard deviation over mean), also averaged over these rows and time of interest. The relative fluctuation level is $\sim$100% at $\sim$3–5 cm outside the separatrix, which is typical of a positively skewed and blob-dominated SOL (see below). The low signal level threshold level of ten camera units at which the normalized pixels are excluded is 0.1 on this scale, which occurs only outside a radius of 10 cm in this shot.

Figure 3 shows the time dependence of typical normalized GPI signals for a single pixel at 3 cm outside the separatrix at the vertical middle of the image (40th row). Figure 3(a) is for an Ohmic shot with a relatively large number of excursions above the blob threshold level of $T = 3$ (#138 121), and Fig. 3(b) is for an H-mode shot with relatively few such excursions (#141 324). Recall from Sec. II C just above Eq. (1) that, for this paper the blob fraction is defined as the fraction of time that the *normalized* GPI signal is above a threshold level of $T = 3$, averaged over the spatial region of interest in the SOL. The blob fractions for these shots as defined in Eq. (1) were $f_b = 4.7\%$ for the Ohmic shot #138 121 and $f_b = 0.6\%$ for the H-mode shot #141 324 (see Table I), so that this Ohmic shot had a blob fraction of about $8\times$ that for the H-mode shot, averaged over the blob analysis region. This Ohmic shot had the third from the highest blob fraction in the 103-shot database (the highest shot having $f_b = 4.8\%$), while this H-mode shot had the fourth from the lowest blob fraction in this database (the lowest shot having $f_b = 0.1\%$). The L-mode shot of Figs. 1 and 2 had an intermediate blob fraction of $f_b = 3.2\%$. Videos of raw GPI data from these shots are shown in the supplementary material.

Figure 4 shows the PDF of the normalized GPI signals for the two shots used in Fig. 3, along with the averaged PDF for the whole 103-shot database. Each pixel in the blob analysis zone of Fig. 1(d) for each frame within the time of interest is counted for these distributions, except for pixels with very low signal levels, as discussed above. The Ohmic shot #138 121 clearly has relatively more pixels above the blob threshold of $T = 3$ than the H-mode shot #141 324. These two shots are near the extremes of high and low blob fraction, as mentioned above, while the PDF for the 103-shot average is in-between the two. All three of these PDFs show clear positive skewness characteristic of blobs in the SOL, which is qualitatively similar to that in MAST,[4] DIII-D,[19] and other tokamaks.


FIG. 2. Radial profiles of the GPI signal level (red), the blobs (blue), and the relative GPI signal fluctuation level (green), all averaged over the poloidal region in the white box of Fig. 1(d) for shot #142 270. The average GPI signal peaks $\sim$1 cm inside the separatrix, while the relative number of blobs—i.e., the relative number of pixels with normalized signal level ≥ 3—peaks at $\sim$2–4 cm outside the separatrix, where the GPI fluctuation level (std/mean) is also the highest. The blob fraction averaged over the blob zone is $f_b = 3.2\%$ for this shot.


FIG. 3. Time dependence of the normalized GPI signal levels for two shots for a single pixel at 3 cm outside the separatrix at the vertical middle of the image (40th row). (a) Ohmic shot with a relatively large number of events above the blob threshold level of $T = 3$ (#138 121). (b) H-mode shot with relatively few events above $T = 3$ (#141 324). The Ohmic shot had about $8\times$ the number of such frames above $T = 3$ than the H-mode shot, i.e., an $8\times$ larger blob fraction, averaged over the blob analysis region.
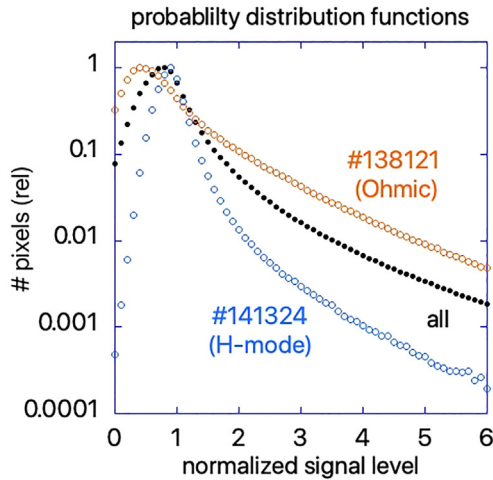
FIG. 4. The PDF of the normalized GPI signals for the same two shots as in Fig. 3, along with the shot-averaged PDF for the entire 103-shot database. Each pixel in the blob in the blob analysis region for each frame during the time of interest is counted for these distributions, except for noisy pixels with very low signal levels as discussed above. The Ohmic shot has relatively more pixels above $T = 3$ than the H-mode shot, with the average over all shots being somewhere in between.

Given the smoothly varying shapes of the PDFs in Fig. 4, there is no unique choice for the threshold level "T" to define a blob in these data (see Sec. I). Thus, for simplicity and definitiveness, a threshold criterion of $T = 3$ for the normalized GPI signals will be used to estimate the blob fractions in this paper, as discussed in Sec. II C. The qualitative results are not very sensitive to this choice, as can be seen in Fig. 5, where the average fraction of pixels above $T = 2$ and $T = 4$ is plotted vs the $T = 3$ fraction for all 103 shots in the database.
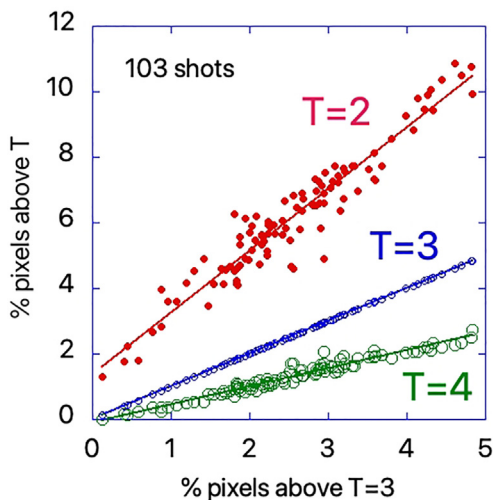
FIG. 5. The average fraction of pixels above $T = 2$ and $T = 4$ in the blob zone is plotted vs the $T = 3$ fraction for all 103 shots in the database. The fraction of pixels above $T = 2$ is about twice that for $T = 3$, and the fraction for $T = 4$ is about half that for $T = 3$.

The fraction of pixels above $T = 2$ is about twice that for $T = 3$, and the fraction for $T = 4$ is about half that for $T = 3$. The cross correlation coefficients between the $T = 3$ data and the $T = 2$ and $T = 4$ data are 0.96 and 0.98, respectively, showing that these three measures have nearly the same relative ordering of the blob fractions for these shots.

The fraction of normalized GPI pixels above the chosen blob threshold level of $T = 3$ (see Sec. II C) and within the blob analysis zone and time of interest was evaluated for each of the 103 shots in this database. In the following, we call this the blob fraction f_b, which is a single number evaluated for each shot, as defined in Eq. (1). Of course, this blob fraction depends on the definition of a blob, and so is best viewed as providing a *relative* measure of the blob fraction for each NSTX shot in this database. These blob fractions in this database ranged over $f_b = 0.12\%$–4.84%, with an average of 2.5%. Estimates of the uncertainties and sensitivities of these blob fractions are discussed in Appendix A. The best uncertainty estimate was made using subgroups of six or more shots on the same run day with similar (but not identical) plasma parameters. The standard deviation of the blob fraction within a given subgroup ranged from 0.3% to 0.7% (see Table III in Appendix A), so a rough estimate of the uncertainty in these blob fractions is $\pm 0.5\%$.

The correlation of these blob fractions with various plasma parameters was made using the standard normalized correlation coefficient between two sets of n parameters x_n and y_n as follows:

$$C(x_n, y_n) = \sum (x_n - \langle x_n \rangle)(y_n - \langle y_n \rangle) / \sqrt{\left(\sum (x_n - \langle x_n \rangle)^2 \sum (y_n - \langle y_n \rangle)^2 \right)}, \quad (2)$$

where $\langle x_n \rangle$ and $\langle y_n \rangle$ are averages over the set of n shots. This correlation coefficient is near 1.0 if the two sets of data go above and below their averages together, near -1.0 if one variable goes up when the other goes down, and near 0 if these parameters are uncorrelated (see below).

Figure 6 shows the blob fractions for all 103 shots in this database as a function of their global plasma parameters. Figures 6(a) and 6(b) show the dependence of f_b on the NBI power P_{NBI} and plasma stored energy W, along with linear fits to these data (straight lines). There is a significant negative correlation between the blob fractions and these two parameters, with a cross correlation coefficient averaged over all shots of -0.48 and -0.47, respectively, as shown in Table II. A negative correlation coefficient here means that the blob fraction decreases with increasing P_{NBI} and W. This trend of decreasing relative blob fraction with increasing NBI power and stored energy was also seen in the Ohmic and H-mode examples of Figs. 3 and 4, although some H-mode shots have f_b above those for Ohmic plasmas and *vice versa* (see Sec. III C).

Figure 6(d) shows a similar correlation of -0.51 between the blob fraction and the outer midplane gap, which is related to the outer midplane separatrix radius by outer gap $= 157.5$ cm-R_{sep} (the outer midplane separatrix). A larger blob fraction is generally observed with decreasing distance of the outer plasma edge to the midplane limiter. Note that the blob analysis region moves radially with the local separatrix in the GPI field of view and, so, retains a radial width of 7.5 cm for all shots. There is also a significant -0.48 correlation of the blob fraction with the line-averaged density, as shown in Fig. 6(e). The other
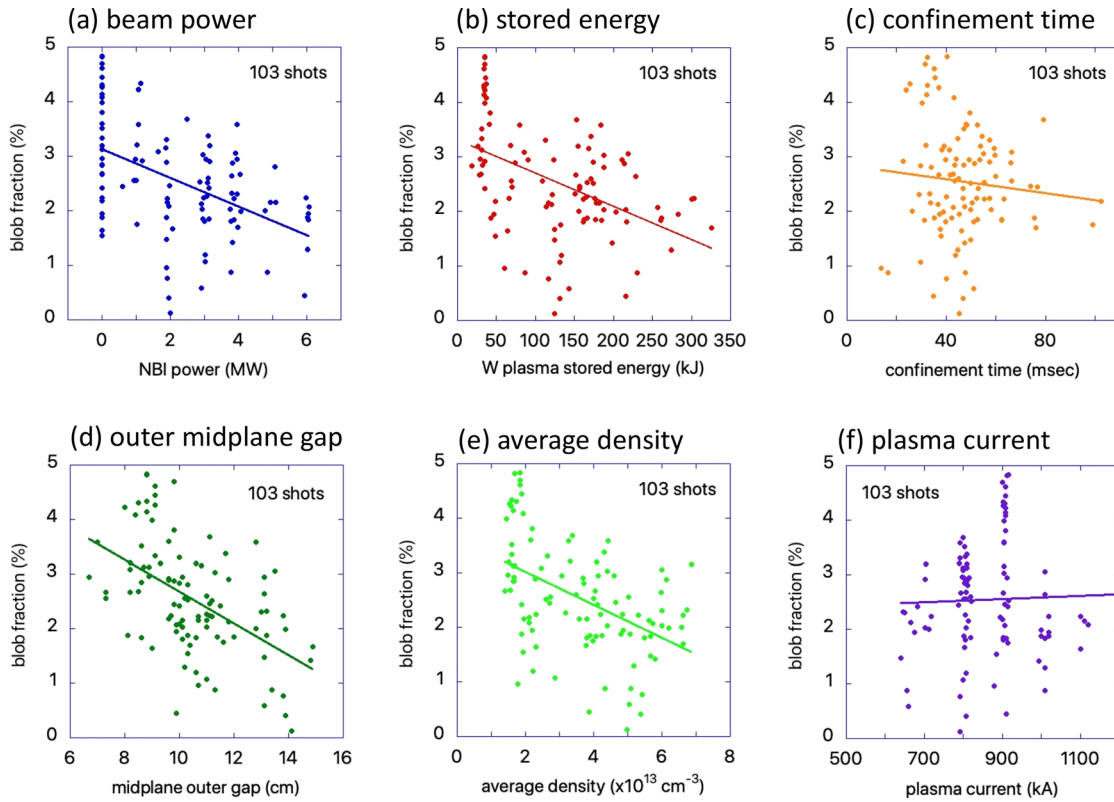
FIG. 6. Dependence of the blob fraction f_b (i.e., the percentage of normalized GPI pixels above T = 3) for six global discharge parameters for each of the 103 shots in this database, along with linear fits (straight lines). The blob fraction dependences are shown as a function of (a) the neutral beam power, (b) the plasma stored energy, (c) the plasma confinement time, (d) the outer midplane gap, (e) the line-averaged plasma density, and (f) the plasma current. There is a moderately high correlation magnitude of 0.47–0.51 between the blob fraction and the density, beam power, stored energy, and midplane outer gap parameters, as shown in Table II.

TABLE II. Blob fraction correlations with plasma parameters.

Parameter	f_b correlation
NBI power	−0.48
Stored energy	−0.47
Confinement time	−0.09
Outer gap	−0.51
Average density	−0.48
Plasma current	0.03
Toroidal field	−0.21
T_e at −5 cm	−0.45
n_e at −5 cm	−0.43
V_{pol} at −3 cm	0.61
V_{rad} at −3 cm	0.02
Grad V_{pol} (neg)	−0.61
Grad V_{pol} (pos)	−0.39
τ_{auto} (μs)	0.03
L_{rad}/L_{pol}	−0.33
Eq. (6) criterion	0.43

dependences in Fig. 6 are relatively weak: −0.09 with energy confinement time in (c), and 0.03 with plasma current in (f). There is also a low correlation of f_b with the toroidal field B of −0.21 (not shown). The dependence of f_b on Ohmic vs H-mode edge conditions will be discussed in Sec. III C.

The statistical significance of the correlations of Table II can be judged by a numerical experiment that correlated 10 000 sets of 100 random pairs of numbers, corresponding to a 100-shot database. The mean of the absolute value of these paired correlations was 0.08, with 32% of the runs having a correlation ≥ 0.1, 4% having a correlation ≥ 0.2, and only 0.2% having a correlation ≥ 0.3. Thus, the four highest correlation coefficients ≥ 0.48 mentioned above are highly unlikely to have occurred at random.
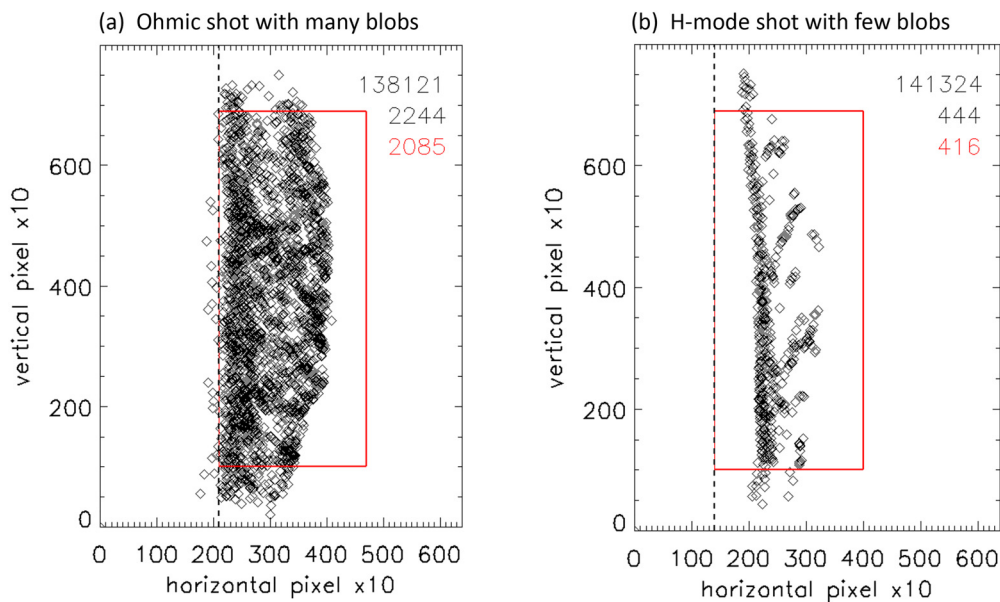
Although there is a statistically significant correlation of blob fractions with the NBI power, stored energy, the outer midplane gap, and the average density, the results of Fig. 6 and Table II do not identify a single dominant correlate for the large variation in relative f_b among the shots in this database, which ranges from about $f_b = 0.1\%$ to 5%. This motivates a check of these results using alternative blob definitions in Sec. III B, and a search for additional correlations using the local parameters from Thomson scattering and GPI velocimetry in Secs. III C and III D.

B. Blobs from contour mapping

The analysis in Sec. III A measured the blob fraction in each shot as the number of pixels above a threshold of T = 3 in the normalized GPI signal. In this section, we describe an alternate analysis in which individual blobs are identified by contour mapping in the image plane, as described in Sec. II C. Only closed contours were counted as blobs when their centers lay within the blob zone shown in Fig. 1(d) and when they had a contiguous area of $\geq 1.4\,cm^2$ above a normalized signal level of T = 3. This way, the number of individual blobs in each frame of each shot can be added up and the total number cross-correlated with the plasma parameters.

Note that there is no attempt here to track the motion or lifetime of blobs from frame-to-frame, just as there was no such blob tracking used in the first (T = 3 PDF threshold) method of Sec. III A. The blob fraction of Sec. III A and the blob contour mapping method in this section average over all blob locations and provide a measure of the relative probability of blobs within a consistent region of space and time for each shot.

Figure 7 shows the locations of all of the blob centers in all frames of the GPI image plane for the two sample shots of Fig. 3 over the 10 ms time of interest. In figure (a) is the Ohmic shot #138 121 with relatively many blobs, and in figure (b) the H-mode shot #141 324 with relatively few blobs, as described in Table I. In the Ohmic shot in figure (a), there were a total of 2244 blobs, 2085 of which had centers inside the blob analysis zone shown by the red box, while in the H-mode shot there were 444 blobs, 416 of which had centers inside the red blob zone. For the Ohmic shot, 35% of the ∼4000 frames had no blobs, 54% had one blob, 10% had two blobs, and 1% had three blobs. The corresponding fractions for the H-mode shot were 89%, 10%, 1%, and 0% for 0, 1, 2, and 3 blobs/frame, respectively.

Figure 8 shows a comparison between the blob analyses done using blob contour mapping and the PDF threshold method of Sec. III A for all 103 shots in the database. Figure 8(a) shows the average blob area/frame for blobs with centers inside the red zone of Fig. 7 vs the blob fraction. These two blob measures have a high (96%) cross correlation and produce very similar blob area results, since a blob fraction of 5% within the analysis zone corresponds to an area of 7.5 × 22.5 cm^2 × 0.05 = 8.4 cm^2, which is close to the extrapolated value of 7.5 cm^2 at 5% blob fraction of the data in Fig. 8(a). The small differences between these two blob measures are due to blob contours with area ≤ 1.4 cm^2 (which are counted in the PDF measurement), and to blobs with centers inside the blob zone extending outside that zone (which are counted in the area measurement). The correlations between the blob area/frame and the plasma parameters are similar to those for the blob fractions shown in Table II; for example, the correlations of blob area with the NBI power and stored energy are −0.50 and −0.54, compared with −0.48 for the blob fraction for both.

Figure 8(b) shows the average number of blobs/frames inside the red zone of Fig. 7 vs the blob fraction for all 103 shots in the database. These two measures of blobs have a somewhat lower cross correlation (0.79), perhaps because of a varying area/blob for these shots, which ranges from 5 to 21 cm^2 with a shot-average area/blob of 12.3 cm^2. The correlations between the average number of blobs/frames and the plasma parameters are similar to those for the blob fractions shown in Table II; for example, the correlations of blob area with the NBI power and stored energy are −0.52 and −0.60, compared with −0.48 for the blob fraction.

The conclusion from this section is that the blob analysis done using 2D contours produces similar (although not identical) results as the PDF threshold method of blob fractions of Sec. III A. Thus, for the rest of this section, only the results from the PDF threshold method will be used.
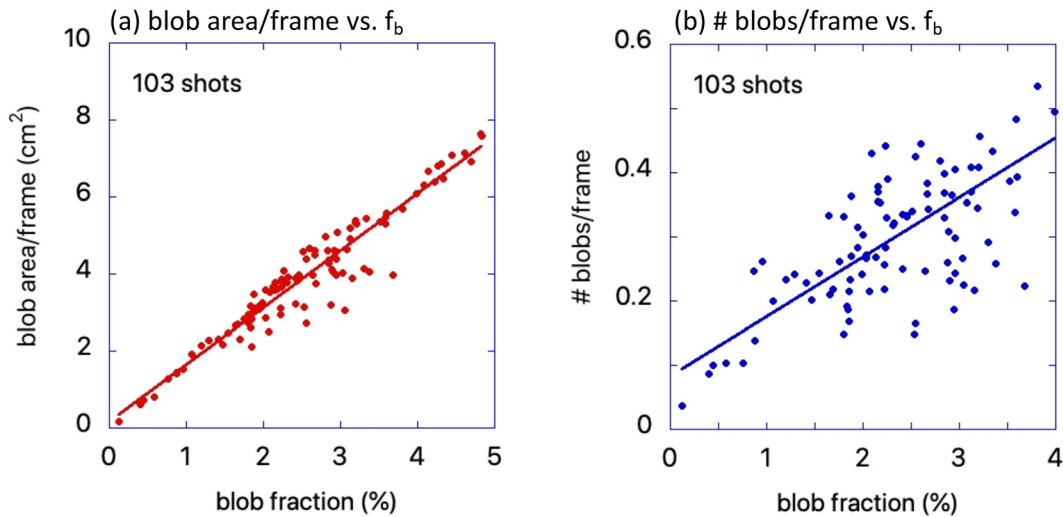

FIG. 7. Location of all the blob centers in all frames of the GPI image plane based on contour mapping for the two sample shots of Fig. 3 and Table I over the 10 ms time of interest. (a) Ohmic shot #138 121 and (b) H-mode shot #141 324. Almost all of the blob centers are within the zone from 0 to 7.5 cm outside the separatrix, as defined by the red box [same as in Fig. 1(d)]. There were 2085 blobs in the red blob zone in shot (a) and 416 in shot (b) over these ∼4000 frames.

FIG. 8. Comparison between blob analysis done using contour mapping and the PDF threshold for all 103 shots in the database. Only closed contours were counted as blobs when they had a contiguous area of $\geq 1.4\,cm^2$ above the normalized threshold level of $T = 3$. (a) Average blob area/frame vs the fraction of pixels above $T = 3$, which shows a high 0.96 correlation. (b) Number of blobs vs the fraction of pixels above $T = 3$, which shows a moderate 0.79 correlation.

C. Blob fraction vs edge parameters

Since there was only a moderately high correlation of about 0.5 between the blob fractions and the global plasma parameters as shown in Fig. 6 and Table I, it is interesting to see if the local edge parameters correlate better with f_b. It would also be more physically meaningful to relate SOL blobs with edge rather than global parameters; for example, blob formation has previously been linked in theory to the region of velocity shear[17,18] or to the maximum pressure gradient.[32]

The edge electron temperature and density were measured with Thomson scattering at the outer midplane on 102/103 shots in this database. Examples of the Thomson scattering profiles for the two sample shots of Fig. 3 at the times nearest the peak GPI signal are shown in Fig. 9, with the electron density in Fig. 9(a) and the electron temperature in Fig. 9(b). As usual, the Ohmic #138 121 shot has a relatively low edge density and temperature and the H-mode shot #141 324 has a higher edge density and temperature with an edge pedestal. These profiles were spline fit to interpolate between the measured points, and a database of the values at −5 cm inside the separatrix was created. This location is shown by the dashed (for Ohmic) and solid (for H-mode) vertical lines in Fig. 9. This is at the top of the edge density pedestal for the H-mode case.
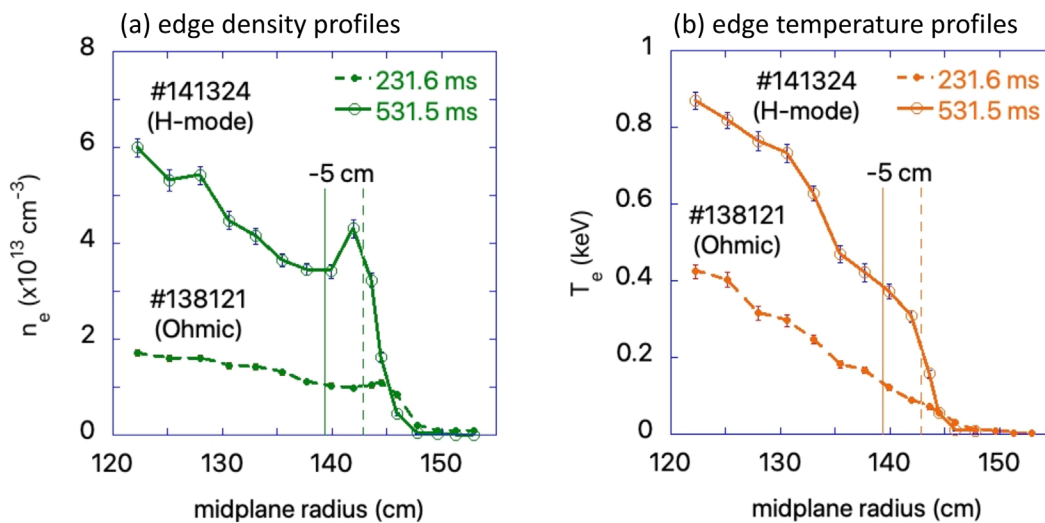
FIG. 9. Thomson scattering edge profiles for the two sample shots at the times nearest the peak GPI signal, with the electron density in figure (a) and the electron temperature in figure (b). The Ohmic #138 121 shot (dashed line) has a relatively low density and temperature and the H-mode shot #141 324 (solid line) has a higher density and temperature with a high edge density pedestal. The radial locations at −5 cm inside the separatrix are shown by dashed and solid vertical lines for Ohmic and H-mode cases, respectively.

Figure 10 shows the relationship between the blob fraction and the electron density and temperature at -5 cm inside the separatrix for 102/103 shots in this database. The points with $n \geq 2.7 \times 10^{13}$ cm^{-3} and $T_e \geq 0.15$ keV are H-mode shots, identified by their large edge density and density gradient, and indicated by the filled symbols (58 shots). Almost all (56/58) of the H-mode shots have NBI power ≥ 1.8 MW. The shots with the lowest blob fractions $f_b < 1.5\%$ were almost all H-mode and the shots with the highest blob fractions $f_b > 3.5\%$ were almost all Ohmic; but, for intermediate blob fractions $f_b = 1.5\%$–3.5% there were both H-mode and Ohmic shots. This mixture resulted in the moderate correlation of -0.43 to -0.45 between these densities and temperatures and the blob fraction, as shown in Table II, with an average blob fraction of $f_b = 2.1 \pm 0.8\%$ for the H-mode shots and $f_b = 3.1 \pm 1.0\%$ for the Ohmic/L-mode shots. Note that within either the H-mode or Ohmic shots taken separately, there appears to be little variation in f_b over this whole range.

Other potential relationships between the Thomson data and the blob fractions were also examined but not shown in Table II. The correlation of the electron pressure (density times temperature) at -5 cm with the blob fraction was -0.44, and the correlation of f_b with electron collisionality ($n_e T_e^{-1.5}$) at -5 cm was -0.27. The correlations of the blob fraction and the n_e and T_e measured at -3 cm inside the separatrix (instead of -5 cm) were -0.42 and -0.43, respectively. The correlations with n_e and T_e measured 16 ms before the time nearest the peak GPI signal used in Fig. 10 were -0.44 and -0.43, respectively. The correlations of the electron density and temperature *gradients* averaged over -5 to 0 cm inside the separatrix were in the same range, since the density and temperature at the separatrix were much smaller than at -5 cm (see Fig. 9). Finally, the small edge density peak ("ear") that occurred in 16/58 shots with the H-mode, such as the one shown in Fig. 9(a), was not significantly correlated with the blob fraction.

The conclusion of this section is that the edge electron parameters were *not* much better correlated with the blob fractions than the most highly correlated of the global parameters such as the NBI power and density. It is also somewhat surprising that for blob fractions in the range 1.5%–3.5% in Fig. 10 (which constitute most of the data), there was a mixture of both Ohmic and H-mode shots. Evidently, shots with H-mode edges do not always have lower blob fractions than Ohmic shots, although there is an overall statistical trend in this direction.

## D. Blob fraction vs edge turbulence velocity

The measured blob fraction in NSTX might be related to the process of blob formation by the velocity shear of edge turbulence, as described, for example, in Refs. 17 and 33. This mechanism presumably applies to the turbulence inside the separatrix where blobs are created, which then propagate into the SOL.

The poloidal and radial edge turbulence velocities were evaluated using a 2D cross correlation technique similar to that described recently.[34] The full 10 ms time series from a single pixel in the normalized image data was cross-correlated with time-delayed time series from all neighboring pixels using a delay time of two frames (5 μs). The location of the maximum of the time-delayed cross correlation coefficients was used to determine the movement of the turbulence in the GPI image plane, i.e., the 2D turbulence velocity was evaluated from the displacement of the maximum of this time-delayed correlation. This analysis was done separately for every radial image column within ± 5 cm of the separatrix starting from the middle row of the image (#40), and these results were averaged with results from rows #30 and #50 in the 80 row images. Note that this analysis did not attempt to identify individual blob structures but uses only the normalized GPI time series. Further details are described in Appendix B.

Figure 11 shows the results of this turbulence velocity analysis for the two sample shots used above: one an Ohmic shot (#138 121) and one an H-mode shot (#141 324). Interestingly, the Ohmic shot has a
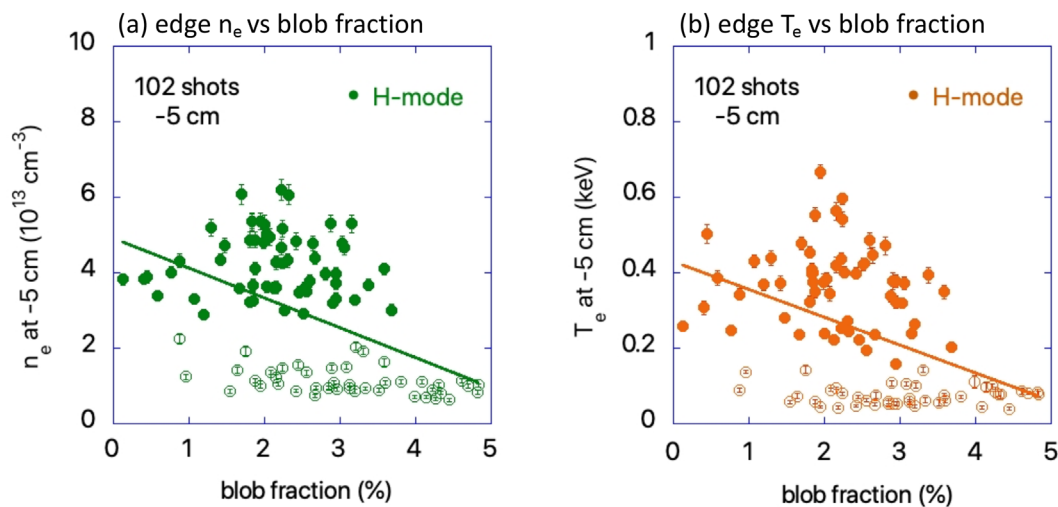
FIG. 10. Relationship between the blob fraction and the edge electron density and electron temperature at -5 cm inside the separatrix for 102/103 shots in the database. (a) Electron density and (b) electron temperature. Shots with H-mode edges are shown by solid symbols. There is a moderately high correlation between the blob fraction and the edge density and temperature, although for a blob fraction of $f_b = 1.5\%$–3.5% there is a wide variation of electron density and temperature. Most of the error bars are smaller than the symbol size. The straight lines are a linear fit through all of the data.
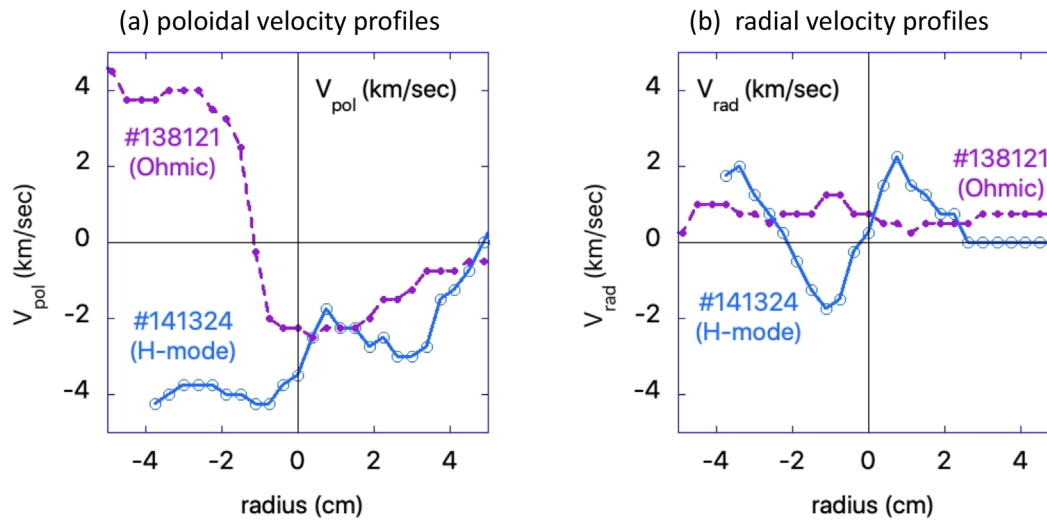
FIG. 11. Sample radial profiles of the turbulence velocity as evaluated using GPI image data. The V_{pol} profiles in figure (a) for the Ohmic shot (#138 121) have more radial shear inside the separatrix than the V_{pol} profiles for the H-mode shot (#141 324). Negative poloidal velocities correspond to rotation in the ion diamagnetic direction. The V_{rad} profiles in figure (b) are radially outward (positive) in the SOL for both shots and nearly flat vs radius for the Ohmic shot.

larger poloidal velocity gradient inside the separatrix than the H-mode shot. The reversal in poloidal turbulence velocity direction from the electron diamagnetic direction inside (positive in this plot) to the ion diamagnetic direction outside the separatrix has been seen before in Ohmic plasmas in NSTX[9] and other tokamaks. The velocity profile in the H-mode case is relatively flat inside the separatrix, even in the region of the pedestal gradient just inside the separatrix shown in Fig. 10.

This measured poloidal velocity of the turbulence in Fig. 11 may be influenced by both the background E × B and diamagnetic velocities. In previous SOLT simulations of an Alactor C-Mod discharge,[35] various measures of the poloidal blob velocity were compared with the E × B, diamagnetic, phase, and group velocities showing a complex relationship in detail, but nonetheless with common trends. These profiles may also be affected by NBI-induced toroidal rotation, which creates an apparent poloidal turbulence velocity in the negative (ion diamagnetic) direction in the GPI field of view. The radial turbulence velocity in Fig. 11(b) is outward (positive) in the SOL, as seen previously in NSTX[9] and many other tokamaks, but it is inward just inside the separatrix for this H-mode shot, as also seen in TCV.[26] We presently have no good theoretical explanation for this inward turbulence propagation.

Figure 12(a) shows the poloidal turbulence velocities V_{pol} for 100/103 shots evaluated at −3 cm inside the separatrix vs the blob fraction as defined in Sec. III A (three shots had the separatrix too near the inner edge of the GPI image to evaluate this velocity). Among the shots with the lowest blob fractions $f_b < 1.5\%$, almost all had a negative V_{pol} corresponding to H-mode plasmas (like #141 324), while almost all shots with the highest blob fractions $f_b > 3.5\%$ had a positive V_{pol} corresponding to Ohmic plasmas (like #138 121). However, for blob fractions of $f_b = 1\%$–3.5%, which comprise most of the data, the V_{pol} could be in either direction. The correlation of the blob fraction with V_{pol} over all 100 shots was 0.61, which is the highest correlation coefficient in Table II. Note that the sign of the V_{pol} values do not directly affect this correlation, just the relative values of V_{pol} with respect to the average of V_{pol} [see Eq. (2)]. The radial turbulence

velocity V_{pol} as shown in Fig. 12(b) was almost always outward at this location, and there was a very low 0.02 correlation between the blob fraction and V_{rad}.

Figure 13 shows the blob fractions vs the maximum and minimum of the radial gradients of the turbulence velocities within the region −3 to 0 cm inside the separatrix. In Fig. 13(a) are the minimum negative (red) and maximum positive gradients (blue) in V_{pol}, and in Fig. 13(b) are the same quantities for V_{rad} (a negative gradient means more negative with increasing radius). The largest minimum negative V_{pol} gradients are for Ohmic plasmas like #138 121, such as shown in Fig. 11(a). The correlation of −0.61 between the blob fraction and the minimum negative gradient of V_{pol} is relatively high, as shown in Table II, while the correlation of −0.39 with the maximum positive gradient of V_{pol} is lower. Figure 13(b) shows that the blob fractions do not vary significantly with the positive or negative gradients in V_{rad}, with both correlations below 0.15 (not shown in Table II).

In addition, when the minimum negative and maximum positive gradients in V_{pol} and V_{rad} were evaluated over the radial range of 0 to +3 cm in the SOL (instead of −3 to 0 cm as above), the correlations with the blob fraction were all below 0.2 (not shown in Table II).

In conclusion, a significant correlation of 0.61 was found between the blob fraction and the turbulence poloidal velocity inside the separatrix, as shown in Fig. 12(a), and a similarly high correlation of −0.61 was found between the blob fraction and the maximum negative gradient of the turbulence poloidal velocity inside the separatrix, as shown in Fig. 13(a). In other words, shots that have a large positive V_{pol} inside the separatrix or have a large negative V_{pol} gradient inside the separatrix have a lower blob fraction. A possible cause for this correlation is discussed further in Sec. IV C.

IV. DISCUSSION

This section discusses the results and their possible theoretical interpretations. Section IV A gives a summary of the blob fraction correlations, Sec. IV B discusses how blob fractions might be understood
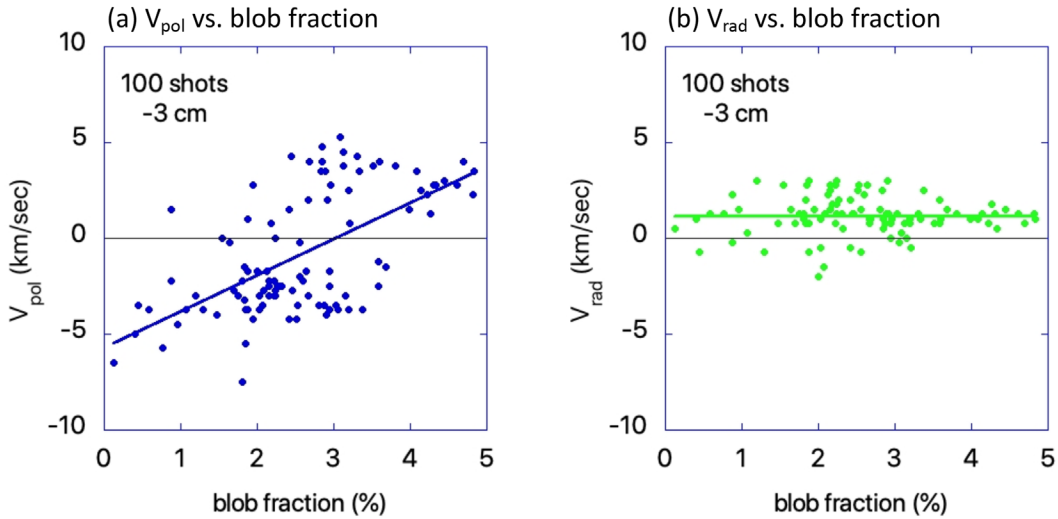
FIG. 12. Turbulence velocities for 100/103 shots evaluated at $-3\,cm$ inside the separatrix vs the blob fraction. The poloidal velocity V_{pol} is shown in figure (a) and the radial velocity V_{rad} is shown in figure (b). The shots with low blob fractions have a large negative V_{pol} corresponding to H-mode shots like #141 324, while the shots with high blob fractions have a large positive V_{pol} corresponding to Ohmic shots like #138 121. The correlation of the blob fraction with V_{pol} was a relatively high, 0.61, but the correlation of the blob fraction with V_{rad} was a low, 0.02 (see Table II). The straight lines are linear fits through the data.

theoretically, Sec. IV C compares the measured blob fractions with a blob birth model, and Sec. IV D discusses the relationship of the blob fraction to the intermittency parameter of statistical theories. Sections IV E and IV F present results of the blob fraction in reduced model computer turbulence simulations for the NSTX and Aditya-U devices, and Sec. IV G discusses ways in which the theory–experiment connection might be improved.

A. Summary of blob fraction correlations

The goal of this paper was to estimate the relative blob fraction for a large database of NSTX shots and to find which plasma parameters were best correlated with this blob fraction. The correlation results are summarized in Table II, which lists seven global plasma parameters, six local edge parameters, along with three parameters related to the blob birth model to be described in Sec. IV C.

The plasma parameters with the highest correlation with blob fraction over this database were the NBI power and total stored energy (-0.47 to -0.48), the outer midplane gap (-0.51), the line-averaged density (-0.48), the turbulence V_{pol} at $-3\,cm$ (0.61), and the maximum turbulence V_{pol} gradient over the range of -3 to $0\,cm$ (-0.61). Plots of these correlations were shown in Figs. 6, 12, and 13. The parameters in Table II with the lowest correlations were the plasma
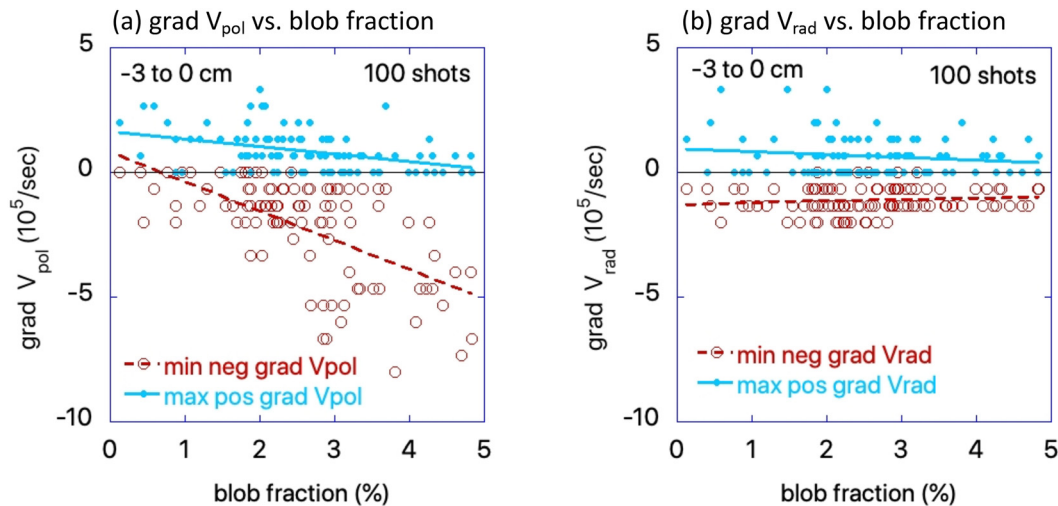
FIG. 13. Radial gradients of the turbulence velocities within -3 to $0\,cm$ inside the separatrix vs the blob fractions. (a) Minimum negative gradients of V_{pol} (red) and maximum positive gradients in V_{pol} (blue) and (b) the same quantities for V_{rad}. The largest gradients are negative for Ohmic plasmas like #138 121, such as shown in Fig. 11(a).

current (0.03), the turbulence V_{rad} at -3 cm (0.02), the confinement time (-0.09), and turbulence autocorrelation time (-0.03).

The clearest simplifying pattern in these correlations is that shots with the lowest blob fraction tended to be H-mode plasmas with relatively high edge density, large negative V_{pol}, and low V_{pol} gradients inside the separatrix, whereas shots with the highest blob fraction tend to be Ohmic shots with relatively low edge density, large positive V_{pol}, and high negative V_{pol} gradients inside the separatrix, as shown in Figs. 11–13. However, in the middle range of blob fractions ($f_b = 1.5\%$–3.5%) there were both H-mode and Ohmic plasmas, so that the overall correlation is only $\sim 60\%$. Thus, there seems to be some hidden variable that determines the blob fraction in this intermediate range. A somewhat surprising result is the decrease in blob fraction with increased outer midplane gap, as shown in Fig. 6(d); however, this gap in this database is fairly well correlated with the NBI power. Of course, the NBI power is well correlated with the stored energy, average density, and the edge parameters due to the dominant effect of NBI heating in high-powered discharges.

It should be noted that the exact value of these correlations depends on the distribution of shot types, which was not explicitly controlled in this database. For example, if nearly all of the shots in the database were Ohmic, then the correlation of blob fraction with NBI would not be strong. Thus, the numerical results of Table II should be considered to be estimates of the blob fraction trends in this NSTX dataset, and not as precise physical correlations.

B. Theory of the blob fraction

The blob fraction defined in this paper, which is also related to the "packing fraction,"[3] is proportional to the blob generation rate and to the duration of time the blob spends in the SOL region under consideration. More precisely, instead of the blob generation rate we should speak of the blob detection rate, since the latter folds in the somewhat arbitrary criterion of what defines a blob at the location of the detection point. The experimental data suggest that the blob radial velocity, if proxied by V_{rad}, is not well correlated with the blob fraction (see Table II and the discussion of Fig. 12). This focuses consideration on how the rate at which blobs are produced and detected is affected by one of the main correlations, velocity shear.

In Sec. IV C, we compare an analytic theory for blob formation by velocity shear with the experimental results on blob fraction. In Sec. IV D, we review an analytic statistical theory of blobs and derive its implications for the blob fraction. In Secs. IV E and IV F, we consider some specific simulation results shedding light on the various roles that velocity shear can play in the formation and release of blobs into the SOL. Mechanisms related to velocity shear include the creation of blobs by the local shearing of streamers, the suppression of turbulence and blob propagation by (zonal or mean flow) shear layers, and the possibility of velocity shear-induced instabilities.

Note that the theoretical blob fractions in this section will be evaluated using electron density fluctuations as a proxy for the GPI signal fluctuations, which is a fairly good approximation in the edge and SOL of NSTX as mentioned in Sec. II A. Note also that for the simulation results in Secs. IV E and IV F, the definition of blob fraction differs from that in Eq. (1) in order to allow better statistics. Although the connections with experiment in this section are qualitative at best, these theoretical results are included to help further the long-term goal of understanding the trends in the data of Sec. III. For a more

quantitative comparison of theory and experiment, the actual NSTX profiles and resulting GPI emission should be used in the simulations, but this is beyond the scope of the present paper.

C. Blob fraction vs analytic blob birth criterion

From earlier calculations[17] using a Taylor expansion of $\mathbf{v}_E \cdot \nabla n$ and retaining the leading radial derivatives of the flow, it can be shown in normalized variables that

$$\frac{1}{n}\frac{\partial n}{\partial t} = \frac{\delta_x}{\delta_y}\frac{(1/B)\partial E_x}{\partial x} + (1/B)\frac{\partial E_y}{\partial x}, \tag{3}$$

where x and y are the radial and poloidal variables, respectively, and $\delta_x = \delta_{rad}$ and $\delta_y = \delta_{pol}$ are the radial and poloidal width of the blob, respectively. Here, the blob velocities are given by the E × B drifts and $(1/B)\partial E_x/\partial x$ and $(1/B)\partial E_y/\partial x$ are proportional to the radial derivatives of the E × B fluid velocities V'_{pol} and V'_{rad}. Parallel losses of blob density are neglected on the short timescale under consideration.

The above equation in terms of the blob formation implies that

$$\frac{\Delta n_b}{n} = \gamma \Delta t_b \left(\frac{\delta_x}{\delta_y}\frac{(1/B)\partial E_x}{\gamma \partial x} + (1/B)\frac{\partial E_y}{\gamma \partial x} \right). \tag{4}$$

Here, γ is the linear growth rate of the plasma interchange turbulence, which is the underlying instability in this model and Δt_b indicates the typical blob formation time from the shearing of a radially elongated streamer. This time should be smaller than the inverse of growth rate γ; $\Delta t_b < 1/\gamma$ since for blob formation the shearing rate is much faster than the interchange growth rate evaluated at the location where the blobs form. Therefore, the parameter $\gamma \Delta t_b$ can be smaller than unity, $\gamma \Delta t_b < 1$. The parameter Δn_b can be related to a density excursion that is greater than some threshold. Using a time-averaged notation, Eq. (4) can be written as

$$\left\langle \frac{\Delta n_b}{n} \right\rangle = \gamma \Delta t_b \left\langle \frac{\delta_x}{\delta_y}\frac{(1/B)\partial E_x}{\gamma \partial x} + (1/B)\frac{\partial E_y}{\gamma \partial x} \right\rangle. \tag{5}$$

The LHS is related to the blob fraction and RHS is associated with the blob formation criterion.

The analytical criterion for blob birth in Ref. 17 related to the RHS of Eq. (5) can be rewritten in terms of NSTX GPI parameters as follows:

$$(V'_{pol}/\gamma)(\delta_{rad}/\delta_{pol}) + V'_{rad}/\gamma > 1. \tag{6}$$

Recently, an initial attempt was made to validate this model using spatially localized and time-resolved GPI analysis for two shots in NSTX.[33] Here, V'_{pol} is the magnitude (absolute value) of the local poloidal velocity gradient, V'_{rad} is the magnitude (absolute value) of the local radial velocity gradient, γ is the linear interchange growth rate, and δ_{rad} and δ_{pol} are the radial and poloidal turbulence correlation lengths, respectively.

A rough estimate of the blob birth criterion in Eq. (6) for the present database can be made using the time-averaged velocity analysis from Sec. III D and comparing the results with the blob fractions of Sec. III A. For each shot, the minimum negative poloidal velocity gradient and minimum negative radial velocity gradient from Fig. 13 were used as proxies for V'_{pol} and V'_{rad} in Eq. (6), since these negative gradients (red in Fig. 13) are larger (on average) than the maximum

positive gradients (blue in Fig. 13). In addition, for each shot the turbulence autocorrelation time τ_{auto} was used a proxy for the inverse growth rate $(1/\gamma)$, and the turbulence correlation lengths L_{rad} and L_{pol} were used as proxies for δ_{rad} and δ_{pol}. These turbulence quantities were calculated from the GPI data for the present database using the methods of Ref. (9) but averaging over the region -3 to 0 cm inside the separatrix. These quantities had shot-averaged values $\tau_{auto} = 11.5\,\mu s$ (HWHM), $L_{rad} = 5.5$ cm (FWHM), and $L_{pol} = 7.5$ cm (FWHM) over the 100 shots with velocity data in this database.

Figure 14 shows the LHS of the criterion of Eq. (6) vs the blob fraction. The averaged value of the LHS of Eq. (6) for these shots is 2.9 ± 1.5, so that almost all shots satisfy the theoretical blob birth criteria in this model, i.e., that the LHS > 1. There is also a fairly clear increase in the blob fraction with this blob birth criterion with a correlation coefficient of 0.43, as shown by the linear fit to the data (straight line). Although this is a statistically significant correlation, it is not larger than the correlations of magnitude 0.6 previously found between the blob fraction and V_{pol} or grad V_{pol} (Table II). This is partly due to the relatively low correlations between the blob fraction and τ_{auto} and L_{rad}/L_{pol}, namely, 0.03 and -0.33, respectively, as shown in Table II.

There are significant uncertainties and limitations in this application of this blob birth model. The evaluation of each term in Eq. (6) has an uncertainty of at least 20%, leading to an overall uncertainty in the left-hand side of order unity. More important is the time-averaging done to evaluate each term, which does not capture the localized process of streamer breaking described by Eq. (6). A separate time-resolved analysis of the GPI data for the two shots shown in red in Fig. 14 (#141 745 and 141 746) showed large space/time variations in the local velocity gradients associated with local blob formation.[33] Therefore, a local space/time evaluation for Eq. (6) for the entire database is desirable, but is beyond the scope of the present paper.
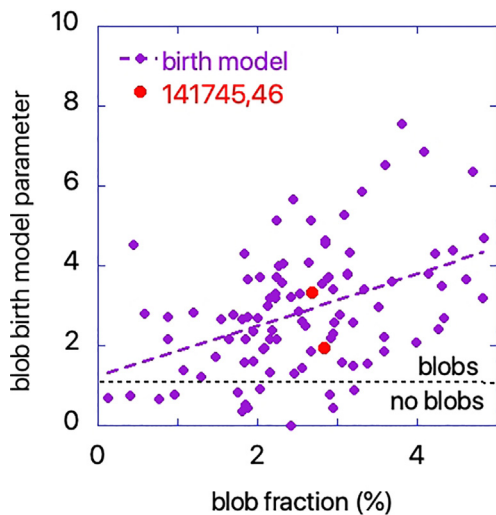

FIG. 14. Blob model criterion evaluated using Eq. (6) for 100 shots in the database vs blob fraction. This blob birth model incorporates both poloidal and radial shear and predicts blob formation if this criterion is >1 on the vertical scale. Almost all points in this database satisfy this criterion. The two points in red are shots analyzed in Ref. 27.

The conclusion from this section is that the blob fraction in the SOL correlates at least qualitatively with the predicted blob birth criterion of Eq. (6). According to this model, the main cause for a high blob fraction is the relatively large poloidal velocity shear for Ohmic plasmas, as illustrated in Figs. 11(a) and 13(a), which tends to create blobs from the breakup of radially elongated streamers. However, the actual streamer structure and blob birth process was not investigated here.

D. Statistical theories

Statistical theories do not directly address the physical mechanisms behind blob formation and propagation; however, as proposed in previous theoretical studies[36] and applied to JET,[37] they provide a framework for calculating the blob contribution to SOL profiles, linking statistical properties to dynamical properties such as blob velocity and lifetime. Thus, the relationship between blob statistics and observations of blob fraction may prove useful for future theoretical modeling.

This section clarifies the relationship between the blob fraction as defined by Eq. (1) and the intermittency parameter used in previously published statistical theories of blobs. By postulating an exponential pulse shape and exponentially distributed pulse amplitudes, it was shown[38] that the PDF of fluctuation amplitudes of a quantity such as density n is given by a gamma distribution, i.e.,

$$P(n) = \frac{\eta}{\langle n \rangle \Gamma(\eta)} \left(\frac{\eta n}{\langle n \rangle} \right)^{\eta-1} \exp\left(-\frac{\eta n}{\langle n \rangle} \right), \quad n > 0 \qquad (7)$$

where the intermittency parameter $\eta = \langle n \rangle^2 / n_{rms}^2$ is also the ratio of duration time of a "pulse" (or "excess event" defined below) to the waiting time between pulses at a particular location. To the best of our knowledge, there is no evidence in the literature supporting or refuting the assumptions of an exponential pulse shape and exponentially distributed pulse amplitudes for GPI signals in NSTX. We retain these idealized assumptions here for expediency, noting that the resulting gamma distribution provides good fits to experimental data from probes in TCV[39] and Alcator C-Mod.[24,40]

The parameter η is closely related to the blob fraction f_b as follows. The fraction of time the signal spends above a particular threshold value T is given by the complementary cumulative distribution function[41] for density fluctuations $1 - C_n(\eta,T)$, where $C_n = \int_0^T dn'\, P(n')$ is the cumulative distribution function. Equating statistics in time with statistics in space as would be the case for constant blob velocity and no blob loss within the region under observation, we have the following:

$$f_b \approx 1 - C_n. \qquad (8)$$

Figure 15 shows the resulting predicted blob fraction as a function of intermittency parameter η for the chosen experimental threshold value of $T = 3$. The highest blob fractions observed in NSTX in the range of 0.04–0.05 correspond to $\eta \approx 1$–1.2 while the lowest blob fractions on the order of 0.0012 correspond to $\eta \approx 4.6$. It is interesting to note that these intermittency parameter estimates for NTSX are not very different from previous estimates for Alcator C-Mod in Ref. 24 where Ohmic discharges have $\eta \sim 0.75$–2 and H-mode discharges have $\eta \sim 3$–5. Thus, the blob fraction results in this paper have a close connection and similarity to studies of intermittency.
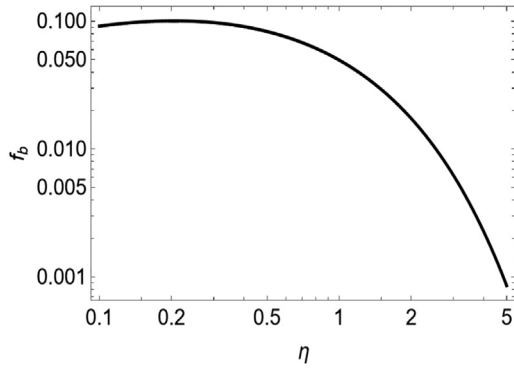
FIG. 15. Predicted blob fraction using Eq. (8) vs intermittency parameter for a threshold value of T = 3.

E. Blob fraction and velocity shear in nSOLT simulations

This section describes the relationship between the blob fraction and the velocity shear as seen in a turbulence simulation made using the reduced model scrape-off layer code nSOLT.[42] This simulation included the addition of an explicit momentum source term $S_{my}(x)$ to the vorticity (charge conservation) equation. The S_{my} source is equivalent to injecting radial current into the plasma,[43] which acts as a control knob for the radial electric field E_r and the associated poloidal E × B velocity and its shear as a function of radial position x. Details of the simulations will be published elsewhere; here, we present the results of a post-processing analysis of the blob fraction.

In the simulation under consideration, which used dimensionless parameters similar to NSTX, the applied S_{my} resulted in a quasi-steady turbulent oscillating state as illustrated in Fig. 16. The lower (red) trace in this figure is proportional to the blob fraction in the SOL. To
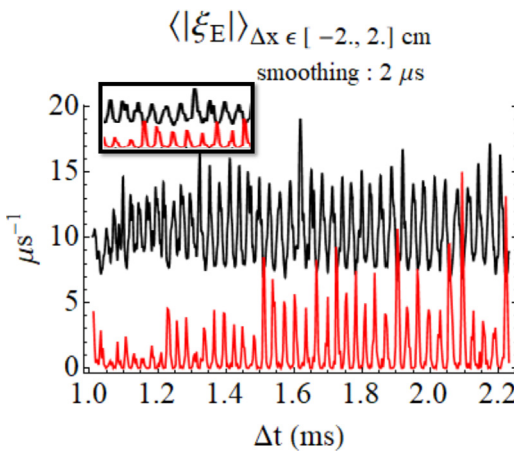

FIG. 16. Lower trace (red) shows the number of fluctuations exceeding a threshold (T = 2) in the SOL (rescaled by dividing by 200) vs time from an nSOLT simulation. The upper trace (black) shows the absolute value of the shearing rate $\xi = |dV_y/dx|$ where y is binormal ($\approx$ poloidal) and x is radial. The inset shows an expanded view near 1.5–1.7 ms. The shearing rate has been averaged over a radial zone of width 4 cm spanning the separatrix.

calculate this, we employed a threshold T = 2 and counted the number of "excess events," i.e., simulation grid points in the SOL for which the normalized fluctuation amplitude exceeded the threshold, i.e., $n/\langle \bar{n} \rangle$ > T in a particular snapshot of time. Note that this definition of blob fraction differs from Eq. (1) in that, here, we do not time average in the numerator because we expect (and observe) the blob fraction to depend on time as the shearing rate varies. Thus, time in our simulations is a proxy for different shots, each with a different condition. Here, $\langle \bar{n} \rangle$ was calculated using both a time and y (binormal) average. Since the time duration of the simulation was much smaller than in the NSTX GPI experiments, we chose a smaller T threshold to increase the number of events and improve statistics. The shearing rate of the poloidally averaged flow, also averaged across a radial zone spanning the separatrix, is shown in the upper trace (black) of Fig. 16. The inset is an expanded view from which it is evident that times of strong (weak) shear correspond to small (large) blob fractions. The correlation between this x-averaged shearing rate and the blob fraction was −0.61. Although the magnitude of the correlation coefficient is similar to the "grad V_{pol} (neg)" correlation in Table II, the interpretation is apparently contrary: in the experiments, the shots with the strongest shear (i.e., strongest negative grad V_{pol} of the turbulence velocity) result in the largest blob fraction. We will return to this point.

Although the strong oscillations shown in Fig. 16 are not seen in the experimental GPI data used in this paper, the oscillations provide a convenient means for a *single* simulation to explore the effect of a range of shearing rates on f_b. In the experiment, shot numbers serve to index the observables that are being correlated, whereas time serves this purpose in the nSOLT simulation.

The anticorrelation between the shearing rate and blob fraction from nSOLT is explored in more detail in Fig. 17, which shows f_b taken over the whole SOL as a function of the shearing rate x in a radial range spanning the separatrix for the same simulation. The main conclusion from the figure is again that small shearing rates are likely to produce a large number of blobs; conversely, blob formation for large shearing rates $\xi > 12 \, \mu s^{-1}$ is rare.

This simulation appears to be oscillating in and out of an H-mode-like state. The near-H-mode conditions may explain the relatively low values of f_b shown in Fig. 17; the time-averaged value was $\langle f_b \rangle \sim 0.9\%$. The threshold, T = 2, rather than the experimentally employed value T = 3, was chosen for our simulation analysis to

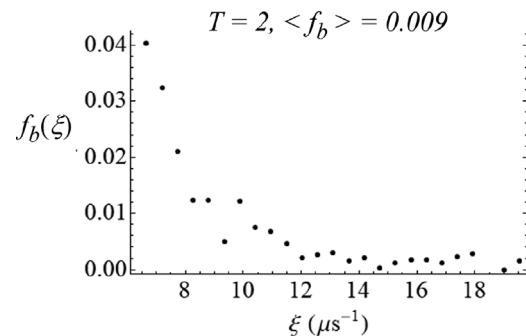**FIG. 17.** The blob fraction f_b in the SOL as a function of the shearing rate averaged over $-2 \, cm < \Delta x < 2 \, cm$ where the separatrix is at $\Delta x = 0$. Results are from the same nSOLT simulation as shown in Fig. 16. The time-averaged blob fraction is 0.9%.

improve statistics. Recall from Fig. 5 that the choice of threshold was argued not to affect qualitative results.

To aid in understanding the diverse effects of shear on the blob fraction, and the possible relationship of these results to experimental results and the blob formation criterion, we examine in Fig. 18 the radial variation of the correlation coefficient between the shearing rate at a given radial location and the blob fraction over the entire SOL. It can be seen that when the shearing rate is measured in the vicinity of the separatrix $\Delta x = 0$, the correlation is negative and substantial in magnitude, in agreement with the previous discussion. However, when the shearing rate is measured near the assumed blob birth zone at $\Delta x \approx -2\,\text{cm}$, which is where the skewness profile vanishes, the correlation with blobs in the SOL is positive—supporting the idea that local shearing is positively correlated with blob formation.

The positive correlation supports the theory of Sec. IV C that blobs are formed near the birth zone by the shearing of streamers. This results in a positive correlation with the birth zone shearing rate. The blobs then propagate radially outward by the usual charge polarization mechanism until they encounter a flow shear layer. In the nSOLT simulations, a strong flow shear layer is located near the separatrix. This shear layer acts as a barrier to blob propagation[44] or can cause its disintegration,[45] preventing the blob's eventual appearance in the SOL. As a result, the correlation coefficient with the shear measured at the barrier location is negative.

Finally, on theoretical grounds, we expect that sheared flows can also drive turbulence through the Kelvin–Helmholtz (KH) instability. Other nSOLT simulations (not shown) support this idea. The KH instability is expected to result in a positive correlation of blobs with shearing rate.

In summary, the role of velocity shear in plasma turbulence as predicted by theory and simulation is complex and diverse. Strong correlations are expected, but with a sign that depends on whether the shear is associated with blob formation, shear layer transport barriers, or KH instability. This complexity may be contributing to the incomplete correlation between the blob fraction and the plasma parameters in Table II and suggests that a more detailed profile analysis of the velocity shear data may be needed in future comparisons with theory.
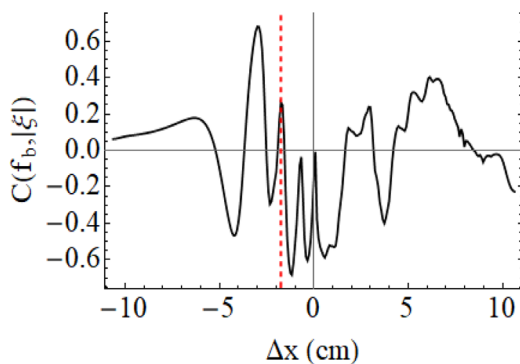
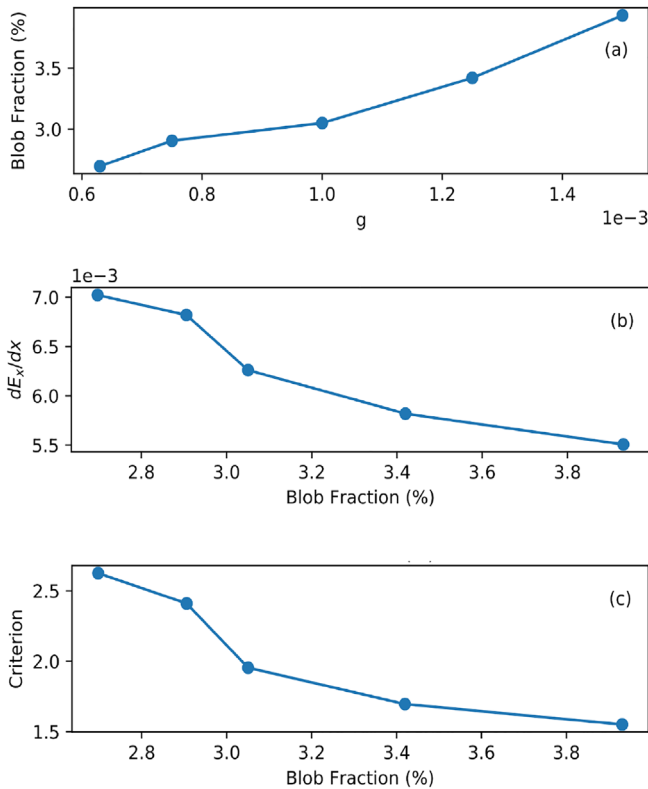### F. Blob fraction in Aditya-U simulation results

In this section, simulation results pertaining to the blob fraction will be discussed based on 2D modeling of interchange modes in the edge and SOL regions. Input parameters for these simulations were taken from the Aditya-U tokamak: $n = 5 \times 10^{12}\,\text{cm}^{-3}$, $T_e = 16\,\text{eV}$ at the last closed flux surface (which are similar to NSTX), $B = 1\,\text{T}$, and $R = 100\,\text{cm}$. Other input parameters and simulation details are given in Ref. 46.

In the simulation analysis that follows, the threshold for a blob has been defined as a fluctuation that exceeds 3.5 times the standard deviation, rather than the $T = 3$ threshold with respect to the mean value as defined in Eq. (1). For these simulations, as for the ones in Sec. IV E, using the threshold criterion of $T = 3$ would result in too few blobs during the duration of the simulations, and hence poor statistics. The blob definition using 3.5 times the standard-deviation results in more blobs when, as here, the standard deviation (std) divided by the mean is relatively low, since (mean $+ 3.5 \times$ std) $< (3 \times$ mean) requires std/mean < 0.57. These blob fractions are intended to illustrate the qualitative trends in the simulations and are not to be compared quantitatively with the experimental results of Sec. III.

Five different numerical simulations have been done using five different magnitudes of the effective gravity $g = c_s^2/R$, which covers the expected range for the edge of Aditya-U. Here, $c_s = (T_e/m_i)^{1/2}$ is the sound speed, and, therefore, g correlates with the edge electron temperature. Since the effective gravity drives the interchange plasma turbulence, the radial electric shear will be different for the five different cases. The radial electric field shear self-controls the turbulence; therefore, the blob fraction and blob formation criterion will be different. Blob formation has been observed from the numerical data; from these data, we have calculated the blob fraction and blob formation criterion. Here, we will present all the results in dimensionless units at a position in the SOL that is 11 ρ_s ($\sim$0.5 cm) outside the separatrix.

Figure 19(a) shows the relative blob fraction as a function of g, where the blob fraction increases with g as high gravity (interchange drive) produces a large number of blobs. The blob fraction as a function of radial electric field shear is shown in Fig. 19(b). The shear decreases the blob fraction; therefore, the rate of blob formation will be lower in the presence of high shear. This result is consistent with the nSOLT results discussed in Sec. IV E in connection with Fig. 17.

Finally, the blob fraction vs the blob birth criterion was investigated in these simulations, similar to Fig. 14. It is found that for high blob fractions, the magnitude of the blob formation criterion decreases, as shown in Fig. 19(c). This trend is opposite to the experimental correlation in NSTX in Fig. 14 and to the analysis in Sec. IV C, but this may be related to the suppression of turbulence and blob propagation by zonal flow shear layers as discussed in Sec. IV E. Fundamentally, the blob formation criterion involves the *local* shearing rate in position and time, where the streamer tips are located and where blob formation is occurring. In contrast, the suppression of interchange instabilities is sensitive to the poloidally averaged, i.e., zonal, flow shear at the location of maximum growth rate, while the suppression of streamer and blob propagation depends on the shear layers between the maximum growth location and the observation point. We speculate that the competition between these effects, as illustrated in Fig. 18, is responsible for the different behaviors in these Aditya-U simulations and in the NSTX analysis of Fig. 14.

FIG. 18. Radial variation of the correlation coefficient between the blob fraction in the SOL and the magnitude of the shearing rate at Δx. Here, $\Delta x = 0$ is the separatrix, and the blob birth zone, denoted by the dashed line, is near $\Delta x = -2\,\text{cm}$ where the skewness profile (not shown) vanishes.

FIG. 19. Simulations of the relative blob fraction in the Aditya-U tokamak. In figure (a), the blob fraction is plotted vs g, where g is normalized by c_s^2/ρ_s, showing the blob fraction increasing with g. Figure (b) shows the effect of radial electric field shear dE_x/dx on the blob fraction, where the blob fraction decreases with increase in shear, and the shear has been calculated using long time and y averages. In figure (c), the blob formation criterion has been plotted as a function of blob fraction.

G. Potential improvements

In general, the present level of agreement between theory and experiment on the blob fraction in NSTX was found to be qualitative at best; so, improvements are needed in order to obtain a more quantitative understanding. Improvements can potentially be made in the measurements, data analysis, and computational simulations.

The measurements of the blob fraction with GPI could be cross-checked with Langmuir probes or a BES-like diagnostic for the SOL. Direct experimental measurement of the electric field shear, which was not available for this dataset, would also be a great aid in future investigations for understanding the applicability of the proposed theoretical mechanisms. We note that electric field shear enters the theory while the poloidal velocity of GPI turbulence discussed in Sec. III D may also have contributions from the diamagnetic velocity, as seen in previous SOLT simulations of an H-mode in Alcator C-Mod, which focused on this issue in greater detail.[35]

Improved data analysis could better quantify the blob birth or detection rate, although this has proven to be difficult and uncertain in the analysis of both experimental data[33] and computational simulations.[47] The product of the blob birth rate and the blob lifetime obtained from 2D blob tracking could provide an alternative measure of the blob fraction.

The simulations described above confirm the sensitivity of blob fraction to the velocity shear, as seen experimentally in NSTX, although the simulations show complex and sometimes different behaviors depending on how they are set up and analyzed. This highlights the need for more dedicated simulations specifically designed to match the NSTX edge profiles and their variations over this database. It would also be useful to compare different types of simulation techniques, e.g., fluid codes vs gyrokinetic codes such as Gkeyll[48] or XGC.[14] Quantitative comparisons with GPI measurements can then be done using a simulation post-processor with a synthetic GPI diagnostic based on the Dα emission rates as a function of density and temperature.[28]

V. CONCLUSIONS

The main results of this paper are the correlation coefficients between the relative blob fractions in the SOL of NSTX and the global and local plasma parameters shown in Table II. The blob fractions had a significant correlation coefficient of −0.47 to −0.48 with the NBI power, stored energy, and plasma density, i.e., the blob fraction was lower for larger values of these parameters. The blob fractions also had a significant correlation coefficient of −0.43 to −0.45 with the edge density and electron temperature, with statistically lower blob fractions in NBI-heated H-modes ($f_b = 2.1 \pm 0.8\%$) than in Ohmic and L-mode plasmas ($f_b = 3.1 \pm 1.0\%$).

The highest correlation coefficients were found between the relative blob fraction in the SOL and the poloidal turbulence velocity (0.61) and its minimum negative radial gradient inside the separatrix (−0.61). This was at least qualitatively consistent with the dependence of blob birth on the local poloidal flow shear of turbulence, as discussed in Sec. IV C. The poloidal turbulence flow shear inside the separatrix can lead (in theory) to a higher blob birth rate and a presumably larger blob fraction in the SOL.

In comparing these results with previous measurements, it should be kept in mind that the relative blob fraction is defined here with respect to the GPI diagnostic data, and so is not exactly the same quantity used to define blobs in the previous experiments. Nevertheless, these results are qualitatively consistent with the (diverse) results from previous experiments, as summarized in Sec. I. For example, in most cases there were fewer blobs in the H-mode than in the L-mode as seen in DIII-D[19] and NSTX,[9,10,20] but there were also many shots with similar blob fractions in the H-mode and L-mode, as seen in ASDEX-Upgrade[21] and TCV.[26] The blob fraction increased here with the poloidal velocity, as in CASTOR,[22] and also correlated with the edge density and temperature, as in ASDEX-Upgrade.[23]

The theoretical discussion in Secs. IV C–IV F suggested several possible mechanisms for understanding the blob fraction results in this paper. The velocity shear criterion for blob birth discussed in Sec. IV C showed a significant but not complete correlation with the blob fraction results for this database. The statistical blob model of Sec. IV D related the blob fraction to the intermittency parameter without any explicit discussion of blob birth. The simulation results of Sec. IV E for NSTX-like edge parameters suggested a more complex and diverse relationship between the velocity shear and blob fraction. Finally, the simulation results of Sec. IV F for Aditya-U parameters showed a blob fraction that increases with the effective gravity and decreases with the radial electric field (i.e., poloidal velocity) shear. More quantitative comparisons of experiment and theory could be made by directly simulating the variation in edge parameters for this

NSTX database and then calculating the resulting blob fractions using a post-processor with a synthetic GPI diagnostic.

SUPPLEMENTARY MATERIAL

See the supplementary material for GPI videos from shots #142 270, 138 121, and 141 324.

ACKNOWLEDGMENTS

AUTHOR DECLARATIONS
Conflict of Interest

The authors have no conflict of interest to disclose.

DATA AVAILABILITY

The data that support the findings of this study are openly available in the PPPL Dataspace Archive at http://arks.princeton.edu/ark:/88435/dsp018p58pg29j, Ref. 49.

APPENDIX A: UNCERTAINTIES AND SENSITIVITIES OF THE BLOB FRACTION

The statistical or random uncertainty in calculating the blob fraction from Eq. (1) is small, given the large number of pixel elements averaged over in each shot: $\sim$4000 image frames with $\sim$1200 pixels in each frame or $\sim5 \times 10^6$ pixels. These image frames contain $\sim$400–2000 two-dimensional blob contours per shot, each with an area of at least 1.5 cm^2 (see Fig. 7). A better estimate of the uncertainty in the blob fraction can be based on the reproducibility or consistency of the blob fraction from shot-to-shot and over time within a shot.

The reproducibility of the blob fraction was evaluated by searching the database for subgroups of shots run on the same day with similar (but not identical) plasma parameters. The variation in blob fraction within these subgroups gives a rough practical estimate of the uncertainty in these blob fractions. There were five such subgroups within this database, as shown in Table III, each subgroup having a different plasma current and toroidal field. The standard deviation of the blob fraction within a given subgroup ranged from 0.3% to 0.7%, as shown in the right-hand column of

TABLE III. Subgroups with similar parameters.

Subgroup	# Shots	P_{NBI} (MW)	W (kJ)	Blob fraction (%)
#138 113–139 126	14	0	34–42	4.3 ± 0.4
#139 044–139 057	6	5.9–6.1	216–303	1.6 ± 0.7
#139 286–139 301	9	3.0–5.1	124–187	2.2 ± 0.7
#138 499–139 510	6	1.9–3.2	155–174	2.7 ± 0.6
#141 740–141 756	11	0	18–32	3.0 ± 0.3

Table III. Since there is also some real shot-to-shot variation within these subgroups, a rough estimate of the uncertainty in the blob fractions in this database is ±0.5%.

Another way to estimate the uncertainty in the blob fraction is to measure its variation over time within a single shot, at least for shots with nearly constant conditions over the GPI gas puff in each shot. The blob fraction is normally evaluated over a ±5 ms time period around the peak signal time, but additional runs of the same blob fraction code were made by averaging over 2 ms time periods from 5 ms before the peak time to 25 ms after the peak time for the three sample shots of Table I, during which times the GPI signal level in the SOL was at least half as large as the peak signal level. The average blob fractions and their standard deviations over these 15 different time intervals for each shot were as follows: $f_b = 4.0 \pm 0.9\%$ for the Ohmic shot #138 121, $f_b = 3.6 \pm 0.6\%$ for the L-mode shot #142 270, and $f_b = 0.5 \pm 0.4\%$ for the H-mode shot #141 324. Since there were five such 2 ms intervals in the normal 10 ms averaging interval, the uncertainty in the normal blob fraction should be smaller by about the square root of 5, i.e., below 0.5% in each case. This is roughly consistent with the 0.5% shot-to-shot uncertainty estimate from Table III.

The blob fraction calculated using Eq. (1) was sensitive to two parameters that were needed to implement that definition of a blob: the radial width of the analysis region and the minimum camera signal threshold used to avoid noisy pixels. We now discuss the sensitivity of the calculated blob fractions to these two parameter choices.

The choice of a radial SOL width of 7.5 cm in Sec. III A was motivated by examples such as Figs. 2 and 7 and a previous analysis[9] showing that most blobs occur between 0 and 7.5 cm radially outside the separatrix. This chosen radial width was varied over a range from 5 cm to 10 cm outside the separatrix for the 103-shot database. The 103-shot-averaged blob fraction (within the corresponding area) was $f_b = 2.5\%$ at 7.5 cm and ranged from $f_b = 2.7\%$ for a 5 cm width to $f_b = 2.1$ for a 10 cm width. The shot-to-shot correlations between the blob fractions for 7.5 cm and the blob fractions for radial widths of 5 and 10 cm outside the separatrix were 0.92 and 0.97, respectively. Thus the blob fractions and their plasma parameter correlations were not very sensitive to the chosen radial width over a ±2.5 cm variation.

The choice of a minimum camera signal threshold was motivated by the desire to avoid small signals in the image, which could be falsely counted as blobs due to random noise in the normalized signals. For Sec. III A, this threshold level was set to 10 for images with a maximum level in the time-averaged images of 125–640. For the chosen SOL width of 7.5 cm, the shot-averaged fraction of pixels below a signal threshold of 10 was 2.9%. When this threshold was changed to 5 and 15, the shot-averaged fraction of pixels below the threshold changed to 0.4% and 10%, respectively. However, the resulting shot-averaged blob fractions only changed from 2.4% to 2.5% to 2.6% over the threshold range 5 to 10 to 15, and the shot-to-shot correlation between the blob fractions at a threshold of 10 to those at 5 and 15 was 0.99 and 0.96, respectively. Thus, the blob fraction was not very sensitive to the choice of threshold over this range.

For this database, there was also a significant shot-to-shot variation in the average camera signal in the edge region due to different SOL plasma parameters and GPI gas puff strengths. For

example, with the standard parameter settings the average signal level in the blob analysis region was 91, but its range over the 103 shots was from 17 to 225. For the 20 shots with the lowest signal levels (below 41), the fraction of excluded pixels below the threshold of 10 was 9%, while for the 20 shots with the highest signal levels (above 126) this fraction was 0%. If this excluded fraction is too high, there will be an artificially *low* blob fraction due to the large number of excluded pixels below threshold. However, the 20 lowest-signal shots had a blob fraction of $3.7 \pm 1\%$ while the 20 highest-signal shots had a blob fraction of 1.9 ± 0.7; so, the signal level does not seem to affect the relative blob fraction in this database. The high-signal shots with a low blob fraction had a much higher stored energy (176 vs 45 kJ) and, so, presumably had a higher average SOL density (not directly measured), which caused the higher GPI signal level. Thus, the lower blob fraction at high signal level and *vice versa* are most likely due to the correlation of the blob fraction with the stored energy and not to the signal level itself.

Finally, an interesting systematic increase was observed in the correlation between the blob fraction and some plasma parameters as the radial analysis width was varied. For example, the correlation between the blob fraction and the V_{pol} at -3 cm varied from -0.61 at a 7.5 cm SOL width (Table II) to -0.50 at a 10 cm SOL width and to -0.72 at 5 cm width. A similar variation was seen for the correlations of blob fraction with the NBI power, stored energy, density, and outer midplane gap [but much less for the blob birth criterion of Eq. (6)]. These plasma parameters were most closely correlated with the blob fraction just outside the separatrix near where the blobs were formed, and these correlations decreased in regions where the blobs were propagating farther into the SOL. The chosen radial analysis width of 7.5 cm characterized the average blob fraction in the SOL, and so somewhat underestimates the maximum correlations found nearer the blob birth zone.

APPENDIX B: TURBULENCE VELOCITY ANALYSIS

The 2D turbulence velocity analysis described briefly in Sec. III D is based on an earlier code used for time-dependent zonal flow analysis.[34] The full 10 ms time series from a single pixel in the normalized image data was cross-correlated with time-delayed time series from all neighboring pixels using a delay time of two frames (5 μs). The location of the maximum of these time-delayed cross correlation coefficients was used to determine the movement of turbulence in the GPI image plane, i.e., the 2D turbulence velocity was evaluated from the displacement of the maximum of this time-delayed correlation.

A key choice in this analysis is the amount of delay time to use. If the chosen delay time is too short, then the movement of the peak can be comparable to a single pixel; but if the delay is too long, the maximum correlation will be low and its location more uncertain. For the two-frame delay used here, the maximum correlations for the examples of Fig. 11 range from 0.78 to 0.98, with the lowest value associated with the largest velocity gradient region in Fig. 11(a). For the 100-shot velocity database at -3 cm in Fig. 12, the maximum two-frame correlations range from 0.67 to 0.99, which is adequately high. Another choice in this velocity analysis is the spatial search range for the maximum correlation. The range chosen

for this analysis was ± 10 pixels in the poloidal (vertical) direction and ± 4 pixels in the radial (horizontal) direction. This range can find velocities of $V_{pol} \leq 15$ km/s and $V_{rad} \leq 6$ km/s, which are well above the observed velocity ranges shown in Figs. 11 and 12.

There are several limitations and uncertainties in this method of velocity analysis in GPI, as discussed in Ref. 34. For the time-averaged analysis over 10 ms used in this paper, any zonal (poloidally oscillating) flows cannot be detected, nor can counter-propagating flows, which seem to be present in some Ohmic plasmas. The toroidal rotation created by the unidirectional NBI in NSTX can create a negative poloidal velocity component in the GPI view, which cannot be distinguished from the poloidal flow. However, the present analysis does give reasonable estimates of the average velocity gradients inside the separatrix, which were useful in the analysis of blob formation, as discussed in Sec. IV C.

REFERENCES

[1] S. I. Krasheninnikov, Phys. Lett. A **283**, 368 (2001).
[2] N. Bisai, A. Das, S. Deshpande, R. Jha, P. Kaw, A. Sen, and R. Singh, Phys. Plasmas **12**, 102515 (2005).
[3] D. A. D'Ippolito, J. R. Myra, and S. J. Zweben, Phys. Plasmas **18**, 060501 (2011).
[4] T. Farley, N. R. Walkden, F. Militello, M. Sanna, J. Young, S. S. Silburn, J. Harrison, I. Kogan, I. Lupelli, S. S. Henderson, A. Kirk, and J. W. Bradley, Rev. Sci. Instrum. **90**, 093502 (2019).
[5] F. Militello, T. Farley, K. Mukhi, N. Walkden, and J. T. Omotani, Phys. Plasmas **25**, 056112 (2018).
[6] D. Carralero, P. Manz, L. Aho-Mantila, G. Birkenmeier, M. Brix, M. Groth, H. W. Müller, U. Stroth, N. Vianello, E. Wolfrum, ASDEX Upgrade Team, JET Contributors, and EUROfusion MST1 Team, Phys. Rev. Lett. **115**, 215002 (2015).
[7] N. Vianello, D. Carralero, C. K. Tsui, V. Naulin, M. Agostini, I. Cziegler, B. Labit, C. Theiler, E. Wolfrum, D. Aguiam, S. Allan, M. Bernert, J. Boedo, S. Costea, H. De Oliveira, O. Fevrier, J. Galdon-Quiroga, G. Grenfell, A. Hakola, C. Ionita, H. Isliker, A. Karpushov, J. Kovacic, B. Lipschultz, R. Maurizio, K. McClements, F. Militello, A. H. Nielsen, I. Olsen, J. J. Rasmussen, T. Ravensbergen, H. Reimerdes, B. Schneider, R. Schrittwieser, E. Seliunin, M. Spolaore, K. Verhaegh, J. Vicente, N. Walkden, W. Zhang, ASDEX Upgrade Team, TCV Team, and EUROfusion MST1 Team, Nucl. Fusion **60**, 016001 (2020).
[8] C. Wang, L. Nie, G. Tang, M. Xu, R. Ke, Y. Chen, H. Wang, Z. Wang, S. Hu, T. Wu, T. Long, Y. Zhu, H. Liu, S. Gong, J. Yuan, and L. Yan, Plasma Sci. Technol. **23**, 055103 (2021).
[9] S. J. Zweben, W. M. Davis, S. M. Kaye, J. R. Myra, R. E. Bell, B. P. LeBlanc, R. J. Maqueda, T. Munsat, S. A. Sabbagh, Y. Sechrest, D. P. Stotler, and NSTX Team, Nucl. Fusion **55**, 093035 (2015).
[10] S. J. Zweben, J. R. Myra, W. M. Davis, D. A. D'Ippolito, T. K. Gray, S. M. Kaye, B. P. LeBlanc, R. J. Maqueda, D. A. Russell, D. P. Stotler, and NSTX Team. Plasma Phys. Controlled Fusion **58**, 044007 (2016).
[11] F. Riva, C. Colin, J. Denis, L. Easy, I. Furno, J. Madsen, F. Militello, V. Naulin, A. H. Nielsen, J. M. B. Olsen, J. T. Omotani, J. J. Rasmussen, P. Ricci, E. Serre, P. Tamain, and C. Theiler, Plasma Phys. Controlled Fusion **58**, 044005 (2016).
[12] P. Paruta, C. Beadle, P. Ricci, and C. Theiler, Phys. Plasmas **26**, 032302 (2019).
[13] X. Q. Xu, N. M. Li, Z. Y. Li, B. Chen, T. Y. Xia, T. F. Tang, B. Zhu, and V. S. Chan, Nucl. Fusion **59**, 126039 (2019).
[14] I. Keramidas Charidakos, J. R. Myra, S. Ku, R. M. Churchill, R. Hager, C. S. Chang, and S. Parker, Phys. Plasmas **27**, 072302 (2020).
[15] G. Decristoforo, F. Militello, T. Nicholas, J. Omotani, C. Marsden, N. Walkden, and O. E. Garcia, Phys. Plasmas **27**, 122301 (2020); G. Dcristoforo, A. Theodorsen, J. Omotani, T. Nicholas, and O. E. Garcia, *ibid.* **28**, 072301 (2021).
[16] F. Nespoli, P. Tamain, N. Fedorczak, G. Ciraolo, D. Galassi, R. Tatali, E. Serre, Y. Marandet, H. Bufferand, and P. Ghendrih, Nucl. Fusion **59**, 096006 (2019).
[17] N. Bisai, S. Banerjee, and A. Sen, Phys. Plasmas **26**, 020701 (2019).
[18] V. Shankar, N. Bisai, S. Raj, and A. Sen, Nucl. Fusion **61**, 066008 (2021).

[19]J. A. Boedo, D. L. Rudakov, R. A. Moyer, G. R. McKee, R. J. Colchin, M. J. Schaffer, P. G. Stangeby, W. P. West, S. L. Allen, T. E. Evans, R. J. Fonck, E. M. Hollmann, S. Krasheninnikov, A. W. Leonard, W. Nevins, M. A. Mahdavi, G. D. Porter, G. R. Tynan, D. G. Whyte, and X. Xu, Phys. Plasmas **10**, 1670 (2003).

[20]M. Agostini, S. J. Zweben, R. Cavazzana, P. Scarin, G. Serianni, R. J. Maqueda, and D. P. Stotler, Phys. Plasmas **14**, 102305 (2007).

[21]G. Y. Antar, M. Tsalas, E. Wolfrum, and V. Rohde, and ASDEX Upgrade Team, Plasma Phys. Controlled Fusion **50**, 095102 (2008).

[22]I. Nanobashvili, P. Devynck, J. P. Gunn, S. Nanobashvili, J. Stöckel, and G. Van Oost, Phys. Plasmas **16**, 022309 (2009).

[23]G. Fuchert, D. Carralero, P. Manz, U. Stroh, E. Wolfrum, and ASDEX Upgrade Team, Plasma Phys. Controlled Fusion **58**, 054006 (2016).

[24]O. E. Garcia, R. Kube, A. Theodorsen, B. LaBombard, and J. L. Terry, Phys. Plasmas **25**, 056103 (2018).

[25]A. Kirk, A. J. Thornton, J. R. Harrison, F. Militello, N. R. Walkden, MAST Team, and EUROfusion MST1 Team, Plasma Phys. Controlled Fusion **58**, 085008 (2016).

[26]C. K. Tsui, J. A. Boedo, J. R. Myra, B. Duval, B. Labit, C. Theiler, N. Vianello, W. A. J. Vijvers, H. Reimerdes, S. Coda, O. Fevrier, J. R. Harrison, J. Horacek, B. Lipschultz, R. Maurizio, F. Nespoli, and U. Sheik, Phys. Plasmas **25**, 072506 (2018).

[27]See https://w3.pppl.gov/~szweben/NSTX%20Blob%20Library/NSTXblobs.html for more examples of blob videos.

[28]S. J. Zweben, J. L. Terry, D. P. Stotler, and R. J. Maqueda, Rev. Sci. Instrum. **88**, 041101 (2017).

[29]S. J. Zweben, E. D. Fredrickson, J. R. Myra, M. Podesta, and F. Scotti, Phys. Plasmas **27**, 052505 (2020).

[30]S. J. Zweben, D. P. Stotler, F. Scotti, and J. R. Myra, Phys. Plasmas **24**, 102509 (2017).

[31]See https://en.wikipedia.org/wiki/Shoelace_formula for information on the shoelace formula.

[32]J. R. Myra, D. A. D'Ippolito, D. P. Stotler, S. J. Zweben, B. P. LeBlanc, J. E. Menard, R. Maqueda, and J. Boedo, Phys. Plasmas **13**, 092509 (2006).

[33]N. Bisai, S. Banerjee, S. J. Zweben, and A. Sen, Nucl. Fusion **62**, 026027 (2022).

[34]S. J. Zweben, A. Diallo, M. Lampert, T. Stoltzfus-Dueck, and S. Banerjee, Phys. Plasmas **28**, 032304 (2021).

[35]D. A. Russell, J. R. Myra, D. A. D'Ippolito, B. LaBombard, J. W. Hughes, J. L. Terry, and S. J. Zweben, Phys. Plasmas **23**, 062305 (2016).

[36]F. Militello and J. T. Omotani, Nucl. Fusion **56**, 104004 (2016).

[37]N. R. Walkden, A. Wynn, F. Militello, B. Lipschultz, G. Matthews, C. Guillemaut, J. Harrison, D. Moulton, and JET Contributors. Plasma Phys. Controlled Fusion **59**, 085009 (2017).

[38]O. E. Garcia, Phys. Rev. Lett. **108**, 265001 (2012).

[39]J. P. Graves, J. Horacek, R. A. Pitts, and K. I. Hopcraft, Plasma Phys. Controlled Fusion **47**, L1–L9 (2005).

[40]R. Kube, A. Theodorsen, O. E. Garcia, D. Bruner, B. LaBombard, and J. L. Terry, J. Plasma Phys. **86**, 095860519 (2020).

[41]A. Theodorsen and O. E. Garcia, Phys. Plasmas **23**, 040702 (2016).

[42]D. A. Russell, J. R. Myra, F. Militello, and D. Moulton, Phys. Plasmas **28**, 092305 (2021).

[43]R. J. Taylor, J.-L. Gauvreau, M. Gilmore, P.-A. Gourdain, D. J. LaFonteese, and L. W. Schmitz, Nucl. Fusion **42**, 46 (2002).

[44]J. R. Myra, D. A. Russell, D. A. D'Ippolito, J.-W. Ahn, R. Maingi, R. J. Maqueda, D. P. Lundberg, D. P. Stotler, S. J. Zweben, J. Boedo, M. Umansky, and NSTX Team, Phys. Plasmas **18**, 012305 (2011).

[45]G. Q. Yu and S. I. Krasheninnikov, Phys. Plasmas **10**, 4413 (2003).

[46]S. Raj, N. Bisai, V. Shankar, and A. Sen, Phys. Plasmas **27**, 122302 (2020).

[47]R. Hacker, G. Fuchert, D. Carralero, and P. Manz, Phys. Plasmas **25**, 012305 (2018).

[48]A. H. Hakim, N. R. Mandell, T. N. Bernard, M. Francisquez, G. W. Hammett, and E. L. Shi, Phys. Plasmas **27**, 042304 (2020).

[49]S. J. Zweben, S. Banerjee, N. Bisai, A. Diallo, M. Lampert, B. LeBlanc, J. R. Myra, and D. A. Russel, see http://arks.princeton.edu/ark:/88435/dsp018p58pg29j for "Correlation between the relative blob fraction and plasma parameters in NST," PPPL Dataspace Archive (2022).